

Numerical analysis of a deep learning formulation of elastic
full waveform inversion with high order total variation
regularization in different parameterization

Tianze Zhang* Jian Sun*[†] Kristopher A. Innanen* Daniel Trad*

* *University of Calgary,*

Department of Geoscience,

Calgary, Alberta, Canada.

[†] *Pennsylvania State University,*

College of Earth and Mineral Science,

University Park, Pennsylvania, USA

(January 25, 2021)

Running head:

ABSTRACT

We have formulated elastic seismic full waveform inversion (FWI) within a deep learning environment. Training this network with a single seismic data set is equivalent to carrying out elastic FWI. There are three main motivations for this effort. The first is an interest in developing an inversion algorithm which is more or less equivalent to standard elastic FWI but which is ready-made for a range of cloud computational architectures. The second is an interest in algorithms which can later (i.e., not in this paper) be coupled with a more involved training component, involving multiple datasets. The third is a general interest in developing the idea of *theory-guiding* within machine learning solutions for large geophysical problems, wherein the number of degrees of freedom within a network, and the

reliance on exhaustive training data, are both reduced by constraining the network with physical rules. In our formulation, a recurrent neural network is set up with rules enforcing elastic wave propagation, with the wavefield projected onto a measurement surface acting as the synthetic data to be compared with observed seismic data. Gradients for iterative updating of an elastic model, with a variety of parameterizations and misfit functionals, can be efficiently constructed within the network through the automatic differential method. With this method, the inversion based on complex misfits can be calculated. We survey the impact of different complex misfits (based on the l_2 , l_1) with high order total variation (TV) regulations on multiparameter elastic FWI recovery of models within velocity/density, modulus/density, and stiffness parameter/density parameterizations. We analyze parameter cross-talk. Inversion results on simple and complex models show that the RNN elastic FWI with high order TV regulation using l_1 norm can help mitigate cross-talk issues with gradient-based optimization methods.

INTRODUCTION

It has recently been shown (Sun et al., 2020) that seismic wave propagation can be simulated with a specialized recurrent neural network (RNN), and that the process of training such a network with a single seismic data set is equivalent to carrying out seismic full waveform inversion (FWI). We are motivated to extend and expand on these results, because of (1) the apparent potential for wider training of such a network to combat common FWI issues such as modelling error; (2) the opportunities for efficient computation (e.g., cloud) offered by FWI realized on platforms like TensorFlow, and (3) an interest in the behavior of more complex RNN-FWI formulations than previously analyzed, e.g., multi-parameter elastic FWI. In this paper we report on progress on the third of these.

The application of machine learning methods to seismic problems has been underway for decades; for example, Röth and Tarantola (1994) presented a neural network-based inversion of time-domain seismic data for acoustic velocity depth-profiles. However, the evolution of these network approaches into deep learning methods, and the results which have subsequently become possible, make many aspects of the discipline quite new, and explain the major recent surge in development and interest. Now, novel seismic applications are being reported in fault detection, denoising, reservoir prediction and velocity inversion (e.g., Jin et al., 2019; Zheng et al., 2019; Peters et al., 2019; Chen et al., 2019; Li et al., 2019a; Smith et al., 2019; Shustak and Landa, 2018). Specifically in seismic velocity inversion, Sun and Demanet (2018) applied a deep learning method to the problem of bandwidth extension; Zhang et al. (2019) designed an end-to-end framework, the velocity-GAN, which generates velocity images directly from the raw seismic waveform data; Wu and Lin (2018) trained a network with an encoder-decoder structure to model the correspondence between

seismic data and subsurface velocity structures; and Yang and Ma (2019) investigated a supervised, deep convolutional neural network for velocity-model building directly from raw seismograms.

The above examples are purely data-driven, in the sense that they involve no assumed theoretical/physical relationships between the input layer (e.g., velocity model) and output layer (e.g., seismic data). We believe that the advantages of the purely data-driven methods are that once the training for the network to perform inversion is finished, take the data-driven training for a network that can perform FWI as an example, the raw seismograms can be directly mapped to the velocity models. This would become a faster inversion method compared with the conventional inversion method that requires iterations. However, seismic inversion is a sophisticated issue, so how we choose the sufficient amount of training data sets that can represent such complex wave physics features and their corresponding velocity models is a hard problem.

Here we distinguish between such methods and those belonging to the *theory-guided* AI paradigm (e.g., Wagner and Rondinelli, 2016; Wu et al., 2018; Karpatne et al., 2017). Theory-guided deep learning networks are, broadly, those which enforce physical rules on the relationships between variables and/or layers. This may occur through the training of a standard network with simulated or synthetic data, which are created using physical rules, or by holding some weights in a network, chosen to force the network to mimic a physical process, fixed and un-trainable. Theory-guiding was explicitly used in the former sense by Downton and Hampson (2018), in which a network designed to predict well log properties from seismic amplitudes was trained not only with real data but with synthetics derived from the Zoeppritz equations. Bar-Sinai et al. (2019) and Raissi (2018) built deep convolutional neural networks (or CNNs) to solve partial differential equations, i.e., explic-

itly using theoretical models within the design, which is an example of theory guiding in the latter sense. Sun et al. (2020), in the work we extend in this paper, similarly set up a deep recurrent neural network to simulate the propagation of a seismic wave through a general acoustic medium. The network is set up in such a way that the trainable weights correspond to the medium property unknowns (i.e., wave velocity model), and the non-trainable weights correspond to the mathematical rules (differencing, etc.) enforcing wave propagation. The output layer was the wave field projected onto a measurement surface, i.e., a simulation of measured seismic data. The training of the Sun et al. (2020) network with a single data set was shown to be an instance of full waveform inversion.

Conventional (i.e., not network-based) seismic full waveform inversion, or FWI, is a complex data fitting procedure aimed at extracting important information from seismic records. Key ingredients are an efficient forward modeling method to simulate synthetic data, and a local differential approach, in which the gradient and direction are calculated to update the model. When updating several parameters simultaneously, which is a multiparameter full waveform inversion, error in one parameter tends to produce updates in others, a phenomenon referred to as inter-parameter trade-off or cross-talk (e.g., Kamei and Pratt, 2013; Alkhalifah and Plessix, 2014; Innanen, 2014; Pan et al., 2018; Keating and Innanen, 2019). The degree of trade-off or cross-talk between parameters can depend sensitively on the specific parameterization; even though, for instance, λ , μ and ρ have the same information content as V_P , V_S , and ρ , updating in one can produce markedly different convergence properties and final models that doing so in the other. The coupling between different physical parameters is controlled by the physical relationships amongst these parameters, and the relationships between the parameters and the wave which interacts with them. Tarantola (1986), by using the scattering or radiation pattern, systematically ana-

lyzed the effect of different model parameterizations on isotropic FWI. He suggested that the greater the difference in the scattering pattern between each parameter, the better the parameters can be resolved. Köhn et al. (2012) showed that across all geophysical parameterizations, within isotropic-elastic FWI, density is always the most challenging to resolve (e.g., Tarantola, 1984; Plessix, 2006; Kamath et al., 2018; Lailly, 1983; Operto et al., 2013; Oh and Alkhalifah, 2016; Pan et al., 2016; Keating and Innanen, 2017).

In RNN-based FWI, then, a natural step is the extension of the Sun et al. (2020) result, which involves a scalar-acoustic formulation of FWI, to a multi-parameter elastic version. Cells within a deep recurrent neural network are designed such that the propagation of information through the network is equivalent to the propagation of an elastic wavefield through a 2D heterogeneous and isotropic-elastic medium; the network is equipped to explore a range of parameterizations and misfit functionals for training based on seismic data. As with the acoustic network, the output layer is a projection of the wave field onto some defined measurement surface, simulating measured data.

In addition to providing a framework for inversion methods which mixes the features of FWI with the training capacity of a deep learning network, this approach also allows for efficient calculation of the derivatives of the residual through automatic differential (AD) methods (e.g., Li et al., 2019b; Sambridge et al., 2007), an engine for which is provided by the open-source machine learning library Pytorch (Paszke et al., 2017). Our recurrent neural network is designed using this library. The forward simulation of wave propagation is represented by a Dynamic Computational Graph (DCG), which records how each internal parameter is calculated from all previous ones. In the inversion, the partial derivatives of the residual with respect to any parameter (within a trainable class) is computed by (1) backpropagating within the computational graph to that parameter, and (2) calculating the

partial derivative along the path using the chain rule.

This paper is organized as follows. First, we introduce the basic structure of the recurrent neural network and how the gradients can be calculated using the backpropagation method. Second, we demonstrate how the elastic FWI RNN cell is constructed in this paper and how the wavefields propagate in the RNN cells. Third, we explain the l_2 and l_1 misfits with high order TV regulation and the mathematical expression for the gradients based on these misfits. Fourth, we use simple layers models and complex over-thrust models to perform inversions with various parameterizations using different misfits. Finally, we discuss the conclusions of this work.

RECURRENT NEURAL NETWORK

A recurrent neural network (RNN) is a machine learning network suitable for dealing with data which have some sequential meaning. Within such a network, the information generated in one cell layer can be stored and used by the next layer. This design has natural applicability in the processing and interpretation of the time evolution of physical processes (Sun et al., 2020), and time-series data in general; examples include language modeling (Mikolov, 2012), speech recognition (Graves et al., 2013), and machine translation (Kalchbrenner and Blunsom, 2013; Zaremba et al., 2014).

[Figure 1 about here.]

[Figure 2 about here.]

Figure 1 illustrates the forward propagation of information through an example RNN, in which each RNN cell represents an instant in time: the $\mathbf{O} = [O_1, O_2, O_3, \dots]$ are the internal

variables in each RNN cell; $\mathbf{S} = [S_1, S_2]$ are the input at each time step; $\mathbf{P} = [P_1, P_2]$ are the output; $\mathbf{L} = [L_1, L_2]$ are the labeled data; and $\mathbf{W} = [W_1, W_2]$ are the trainable parameters at each time step. Mathematical operations relating the internal variables within a cell, and those relating internal variables across adjacent cells, are represented as arrows.

To train this network is to select trainable weights such that labeled data \mathbf{L} and RNN output \mathbf{P} are as close as possible. Specifically, in training we determine the parameters \mathbf{W} , through a gradient-based optimization involving the partial derivatives of the residual with respect to each W_i . These derivatives are determined through backpropagation, which is a repeated application the chain rule, organized to resemble flow in the reverse direction along with the arrows in the network. For the example RNN in Figure 1, this takes the form illustrated in Figure 2, in which the sequence $\mathbf{R} = [R_1, R_2]$ represents the residuals at each time step. Within this example, to calculate the partial derivative of R_1 with respect to W_1 , we back-propagate from node R_1 to W_1 :

$$\frac{\partial R_1}{\partial W_1} = \frac{\partial R_1}{\partial P_1} \frac{\partial P_1}{\partial W_1} = \frac{\partial R_1}{\partial P_1} \frac{\partial P_1}{\partial O_3} \frac{\partial O_3}{\partial W_1} = -2 \quad (1)$$

To calculate the partial derivative of R_2 with respect to W_1 , we backpropagate from R_2 to W_1 :

$$\frac{\partial R_2}{\partial W_1} = \frac{\partial R_2}{\partial P_2} \frac{\partial P_2}{\partial W_1} = \frac{\partial R_2}{\partial P_2} \frac{\partial P_2}{\partial O_5} \frac{\partial O_5}{\partial O_4} \frac{\partial O_4}{\partial O_3} \frac{\partial O_3}{\partial W_1} = -4O_4 \quad (2)$$

If the RNN was set up to propagate through two-time steps, the gradient for W_1 is $-4O_4 + 2$. Real RNNs are more complex and involve propagation through larger numbers of time steps, but all are optimized through a process similar to this. These derivatives are the basis for gradients in the optimization misfit function; using them the \mathbf{W} are updated and iterations continue.

A RECURRENT NEURAL NETWORK FORMULATION OF EFWI

Wave propagation can be simulated using suitably-designed RNNs (Sun et al., 2020; Richardson, 2018; Hughes et al., 2019). Here we take the acoustic wave propagation approach of Sun et al. (2020) as a starting point, and formulate an RNN which simulates the propagation of an elastic wave through isotropic elastic medium. The underlying equations are the 2D velocity-stress form of the elastodynamic equations (Virieux, 1986; Liu and Sen, 2009):

$$\begin{aligned}
 \frac{\partial v_x}{\partial t} &= \frac{1}{\rho} \left(\frac{\partial \sigma_{xx}}{\partial x} + \frac{\partial \sigma_{xz}}{\partial z} \right) \\
 \frac{\partial v_z}{\partial t} &= \frac{1}{\rho} \left(\frac{\partial \sigma_{xz}}{\partial x} + \frac{\partial \sigma_{zz}}{\partial z} \right) \\
 \frac{\partial \sigma_{xx}}{\partial t} &= (\lambda + 2\mu) \frac{\partial v_x}{\partial x} + \lambda \frac{\partial v_z}{\partial z}, \\
 \frac{\partial \sigma_{zz}}{\partial t} &= (\lambda + 2\mu) \frac{\partial v_z}{\partial z} + \lambda \frac{\partial v_x}{\partial x} \\
 \frac{\partial \sigma_{xz}}{\partial t} &= \mu \left(\frac{\partial v_x}{\partial z} + \frac{\partial v_z}{\partial x} \right)
 \end{aligned} \tag{3}$$

where v_x and v_z are the x and z components of the particle velocity, σ_{xx} , σ_{zz} and σ_{xz} are three 2D components of the stress tensor. Discretized spatial distributions of the Lamé parameters λ and μ , and the density ρ , form the elastic model.

[Figure 3 about here.]

In Figure 3 the structure of an RNN cell which produces a staggered-grid finite difference solution for the velocity and stress fields is illustrated. At each time step the discrete sources s_x and s_z act as inputs; the velocity and stress information, $v_x^{t-\frac{1}{2}}$, $v_z^{t-\frac{1}{2}}$, σ_{xx}^t , σ_{zz}^t , and σ_{xz}^t , is communicated between the RNN cells; the partial derivative fields, $\partial_x \sigma_{xx}^t$, $\partial_z \sigma_{zz}^t$, $\partial_x \sigma_{xz}^t$, $\partial_z \sigma_{xz}^t$, $\partial_x v_x^{t+\frac{1}{2}}$, $\partial_z v_x^{t+\frac{1}{2}}$, $\partial_x v_z^{t+\frac{1}{2}}$, $\partial_z v_z^{t+\frac{1}{2}}$ are the internal variables in each RNN cell, which correspond to O in Figure 2; and, λ , μ and ρ are included as trainable weights, which correspond to W in Figure 2. In Algorithm 1 pseudocode detailing these calculations

within the RNN cell is provided. The $*$ symbol represents the machine learning image convolution operator. This image convolution is the process of adding each element of the image to its local neighbors, weighted by the image convolution kernel. We find that this image convolution operator is also capable of calculating space partial derivatives if the convolution kernel is designed according to the finite difference coefficients. Details about the image convolution operation can be found in Podlozhnyuk (2007). dx , dz are the grid intervals, and the image convolution kernels are: $\mathbf{k}_{x_1} = \mathbf{a}/dx$, $\mathbf{k}_{x_2} = \mathbf{b}/dx$, $\mathbf{k}_{z_1} = \mathbf{a}^T/dz$, and $\mathbf{k}_{z_2} = \mathbf{b}^T/dz$, where $\mathbf{a} = [0, 1/24, -9/8, 9/8, -1/24]$ and $\mathbf{b} = [1/24, -9/8, 9/8, -1/24, 0]$. \mathbf{a} and \mathbf{b} are 1×5 dimension arrays. \mathbf{k}_{x_1} and \mathbf{k}_{x_2} are kernels, for the image convolution process, responsible for calculating the staggered grid space partial derivative in x direction. \mathbf{k}_{z_1} and \mathbf{k}_{z_2} are kernels, for the image convolution process, responsible for calculating the staggered grid space partial derivative in z direction, and that is also why the arrays, \mathbf{a} and \mathbf{b} , are transposed in \mathbf{k}_{z_1} and \mathbf{k}_{z_2} . Space partial derivative calculated in this way is, mathematically, the same with conventional staggered grid method (e.g. Virieux (1986)). In this study, we achieve this process in an image convolution way. In algorithm 1, in order to implement the PML boundary, all the stress fields and the velocity fields need to be split into their x and z components. In algorithm 1, d_x and d_z are the PML damping coefficients in x direction and z direction. d_x can be expressed as:

$$d_x(i) = d_{0x} \left(\frac{i}{n_{pmlx}} \right)^p \quad (4)$$

,where $*$ represents either x or z direction. i is PML layer number starting from the effective calculation boundary. n_{pmlx} is the PML layer number in x direction. p is an integer and the value is from 1-4. d_{0x} can be expressed as:

$$d_{0x} = \log\left(\frac{1}{R}\right) \frac{rV_s}{n_{pmlx}\delta_x} \quad (5)$$

,where R is a theoretically reflection coefficient, r is a value ranging from 3-4. δ_x is the grid length in x direction. d_z can also be calculated in the same way.

[Figure 4 about here.]

The activity of the RNN network is illustrated in “unfolded” form in Figure 4. Above the unfolded network, horizontal velocity fields associated with a point source at the top left of a model are plotted at three times during propagation of the wave information through the network, the third being at t_{max} , the maximum receiving time. The wave field values are stored at positions selected to match multicomponent receivers; these form shot records as time evolves, which becomes the output data at each time. These shot records correspond to variables P in Figures 1 and 2, and the observed data. For FWI problem, the observed data is obtained from the true model. For real seismic data inversion, the observed data is obtained from field survey. In this RNN based elastic FWI the observed data is considered as the labeled data. The residuals are calculated at the last computational time as Figure 4 illustrated and this along with a selected norm defines the misfit function used to train the network.

Algorithm 2 describes the training of the network, i.e., the process of elastic RNN FWI. Partial derivatives of the residual with respect to the trainable parameters (in this case λ , μ and ρ) are calculated through backpropagation using the automatic differential method, as set out in the previous section. After we have the gradients then we can use an optimization method and step length to update the trainable parameters and reduce the misfit and start another iteration. In step 4, $RNN()$ is the network discussed above, whose output is the synthetic data; $costFunc()$, in step 5, is the misfit or loss function chosen to measure the difference between the synthetic data and observed data; $loss.backward()$

begins the backpropagation within the computational graph and produces the gradients for each parameter, with which the current parameter model can be updated and another iteration started.

The gradient calculated within the training process above essentially reproduces the adjoint-state calculations within FWI, as discussed by Sun et al. (2020). Formulated as a problem of RNN training, the gradient calculation occurs rapidly and in a manner suitable for cloud computational architectures; also, it allows the researcher to efficiently alter misfit function choices and parameterization in order to do high-level optimization. However, it involves the storage of the whole wavefield, and thus should be expected to have significant memory requirements.

MISFITS WITH HIGH ORDER TV REGULATION

Here we first introduce the elastic RNN misfits based on l_2 norm with high order TV regularization:

$$\begin{aligned} \Phi_{l_2}^{TV}(\mathbf{m}_\lambda, \mathbf{m}_\mu, \mathbf{m}_\rho, \alpha_1^\lambda, \alpha_1^\mu, \alpha_1^\rho, \alpha_2^\lambda, \alpha_2^\mu, \alpha_2^\rho) &= \frac{1}{2} \|\mathbf{D}_{\text{syn}}(\mathbf{m}_\lambda, \mathbf{m}_\mu, \mathbf{m}_\rho) - \mathbf{D}_{\text{obs}}\|_2^2 + \\ &\alpha_1^\lambda \Theta_{\text{TV}}(\mathbf{m}_\lambda) + \alpha_1^\mu \Theta_{\text{TV}}(\mathbf{m}_\mu) + \alpha_1^\rho \Theta_{\text{TV}}(\mathbf{m}_\rho) + \\ &\alpha_2^\lambda \Upsilon_{\text{TV}}(\mathbf{m}_\lambda) + \alpha_2^\mu \Upsilon_{\text{TV}}(\mathbf{m}_\mu) + \alpha_2^\rho \Upsilon_{\text{TV}}(\mathbf{m}_\rho) \end{aligned} \quad (6)$$

,where $\alpha_1^\lambda, \alpha_1^\mu, \alpha_1^\rho, \alpha_2^\lambda, \alpha_2^\mu, \alpha_2^\rho$, are vector of Lagrange multipliers, and $\Theta_{\text{TV}}, \Upsilon_{\text{TV}}$ represents first and second order TV regularization functions respectively. $\mathbf{D}_{\text{syn}}(\mathbf{m}_\lambda, \mathbf{m}_\mu, \mathbf{m}_\rho)$ represents the synthetic data, which is the function of the model parameters, and in this equation they are V_P, V_S and ρ . Θ_{TV} and Υ_{TV} represent functions for calculating the first and second order TV regulations for the models.

The first order TV regulation term can be expressed as:

$$TV_1((\mathbf{m})) = \sum_{i=1}^{n-1} \sum_{j=1}^{m-1} |M_{i+1,j} - M_{i,j}| + \sum_{i=1}^{n-1} \sum_{j=1}^{m-1} |M_{i,j+1} - M_{i,j}| =$$

$$\begin{pmatrix} \nabla_x, \nabla_z \end{pmatrix} \begin{pmatrix} \mathbf{m}, \\ \mathbf{m} \end{pmatrix} = \begin{pmatrix} \mathcal{L}_x, \mathcal{L}_z \end{pmatrix} \begin{pmatrix} \mathbf{m}, \\ \mathbf{m} \end{pmatrix} = \Theta_{TV}(\mathbf{m}) \quad (7)$$

The second order TV regulation term can be expressed as:

$$TV_2((\mathbf{m})) = \sum_{i=1}^{n-1} \sum_{j=1}^{m-1} |M_{i+1,j} - 2M_{i,j} + M_{i-1,j}| + \sum_{i=1}^{n-1} \sum_{j=1}^{m-1} |M_{i,j+1} - 2M_{i,j} + M_{i,j-1}|$$

$$= \begin{pmatrix} \nabla_{xx}, \nabla_{zz} \end{pmatrix} \begin{pmatrix} \mathbf{m}, \\ \mathbf{m} \end{pmatrix} = \begin{pmatrix} \mathcal{K}_{xx}, \mathcal{K}_{zz} \end{pmatrix} \begin{pmatrix} \mathbf{m}, \\ \mathbf{m} \end{pmatrix} = \Upsilon_{TV}(\mathbf{m}) \quad (8)$$

The derivative of $\Phi_{l_2}^{TV}$ for each parameter, which is the gradient for V_P , V_S and ρ based on the l_2^{TV} norm can be expressed as:

$$\begin{pmatrix} \frac{\partial \Phi_{l_2}^{TV}}{\partial \mathbf{m}_\lambda} \\ \frac{\partial \Phi_{l_2}^{TV}}{\partial \mathbf{m}_\mu} \\ \frac{\partial \Phi_{l_2}^{TV}}{\partial \mathbf{m}_\rho} \end{pmatrix} = \begin{pmatrix} \mathbf{G}_{12_\lambda} \\ \mathbf{G}_{12_\mu} \\ \mathbf{G}_{12_\rho} \end{pmatrix} + \begin{pmatrix} \mathbf{R}_\lambda \\ \mathbf{R}_\mu \\ \mathbf{R}_\rho \end{pmatrix} \quad (9)$$

, where $\mathbf{G}_{12_\lambda}, \mathbf{G}_{12_\mu}, \mathbf{G}_{12_\rho}$ are the gradient for λ, μ, ρ . $\mathbf{R}_\lambda, \mathbf{R}_\mu, \mathbf{R}_\rho$ are the regulation terms and the mathematical expressions for these regulation terms are:

$$\begin{pmatrix} \mathbf{R}_\lambda \\ \mathbf{R}_\mu \\ \mathbf{R}_\rho \end{pmatrix} = \begin{pmatrix} \alpha_1^\lambda \mathcal{L}_x^T \mathbf{Q}_{x\lambda} & \alpha_1^\lambda \mathcal{L}_z^T \mathbf{Q}_{z\lambda}, & \alpha_2^\lambda \mathcal{K}_{xx}^T \mathbf{Q}_{xx\lambda} & \alpha_2^\lambda \mathcal{K}_{zz}^T \mathbf{Q}_{zz\lambda} \\ \alpha_1^\mu \mathcal{L}_x^T \mathbf{Q}_{x\mu} & \alpha_1^\mu \mathcal{L}_z^T \mathbf{Q}_{z\mu} & \alpha_2^\mu \mathcal{K}_{xx}^T \mathbf{Q}_{xx\mu} & \alpha_2^\mu \mathcal{K}_{zz}^T \mathbf{Q}_{zz\mu} \\ \alpha_1^\rho \mathcal{L}_x^T \mathbf{Q}_{x\rho} & \alpha_1^\rho \mathcal{L}_z^T \mathbf{Q}_{z\rho} & \alpha_2^\rho \mathcal{K}_{xx}^T \mathbf{Q}_{xx\rho} & \alpha_2^\rho \mathcal{K}_{zz}^T \mathbf{Q}_{zz\rho} \end{pmatrix} \begin{pmatrix} \mathcal{L}_x \\ \mathcal{L}_z \\ \mathcal{K}_{xx} \\ \mathcal{K}_{zz} \end{pmatrix} \cdot \begin{pmatrix} \mathbf{m}_\lambda \\ \mathbf{m}_\mu \\ \mathbf{m}_\rho \end{pmatrix} \quad (10)$$

$$\begin{pmatrix} \mathbf{q}_{x\lambda} & \mathbf{q}_{x\mu} & \mathbf{q}_{x\rho} \\ \mathbf{q}_{z\lambda} & \mathbf{q}_{z\mu} & \mathbf{q}_{z\rho} \\ \mathbf{q}_{xx\lambda} & \mathbf{q}_{xx\mu} & \mathbf{q}_{xx\rho} \\ \mathbf{q}_{zz\lambda} & \mathbf{q}_{zz\mu} & \mathbf{q}_{zz\rho} \end{pmatrix} = \begin{pmatrix} \mathcal{L}_x \\ \mathcal{L}_z \\ \mathcal{K}_{xx} \\ \mathcal{K}_{zz} \end{pmatrix} \begin{pmatrix} \mathbf{m}_\lambda, \mathbf{m}_\mu, \mathbf{m}_\rho \end{pmatrix} \quad (11)$$

$$\begin{pmatrix} Q_{x\lambda} & Q_{x\mu} & Q_{x\rho} \\ Q_{z\lambda} & Q_{z\mu} & Q_{z\rho} \\ Q_{xx\lambda} & Q_{xx\mu} & Q_{xx\rho} \\ Q_{zz\lambda} & Q_{zz\mu} & Q_{zz\rho} \end{pmatrix} = \begin{pmatrix} \frac{1}{|q_{x\lambda}|} & \frac{1}{|q_{x\mu}|} & \frac{1}{|q_{x\rho}|} \\ \frac{1}{|q_{z\lambda}|} & \frac{1}{|q_{z\mu}|} & \frac{1}{|q_{z\rho}|} \\ \frac{1}{|q_{xx\lambda}|} & \frac{1}{|q_{xx\mu}|} & \frac{1}{|q_{xx\rho}|} \\ \frac{1}{|q_{zz\lambda}|} & \frac{1}{|q_{zz\mu}|} & \frac{1}{|q_{zz\rho}|} \end{pmatrix} \quad (12)$$

\mathbf{T} means the transpose of the matrix, \cdot means dot product. $\mathbf{q}_{x\lambda}$ represent the first order TV regularization vector in x direction for parameter λ . $q_{x\lambda}$ represent the values in vector $\mathbf{q}_{x\lambda}$. $Q_{x\lambda}$ is the absolute inverse of $q_{x\lambda}$. $Q_{x\lambda}$ are elements in vector $\mathbf{Q}_{x\lambda}$. $\mathbf{q}_{xx\lambda}$ represent the second order TV regularization vector in x direction for parameter λ . $q_{xx\lambda}$ represent the values in vector $\mathbf{q}_{xx\lambda}$. $Q_{xx\lambda}$ is the absolute inverse of $q_{xx\lambda}$. $Q_{xx\lambda}$ are elements in vector $\mathbf{Q}_{xx\lambda}$. Other values in equations (9) and (10) can be also deduced like this. $\mathcal{L}_x, \mathcal{L}_z$ are the first order differential vector to give the first order total variations in x and z directions respectively. $\mathcal{K}_{xx}, \mathcal{K}_{zz}$ are the second order differential vector to give the second order total variations in x and z directions respectively.

If we were to use $l1$ norm objective function with TV regulation. The objective function can be written as:

$$\begin{aligned} \Phi_{l1}^{TV}(\mathbf{m}_\lambda, \mathbf{m}_\mu, \mathbf{m}_\rho, \alpha_1^\lambda, \alpha_1^\mu, \alpha_1^\rho, \alpha_2^\lambda, \alpha_2^\mu, \alpha_2^\rho) = & \|\mathbf{D}_{\text{syn}}(\mathbf{m}_\lambda, \mathbf{m}_\mu, \mathbf{m}_\rho) - \mathbf{D}_{\text{obs}}\| + \\ & \alpha_1^\lambda \Theta_{\text{TV}}(\mathbf{m}_\lambda) + \alpha_1^\mu \Theta_{\text{TV}}(\mathbf{m}_\mu) + \alpha_1^\rho \Theta_{\text{TV}}(\mathbf{m}_\rho) + \\ & \alpha_2^\lambda \Upsilon_{\text{TV}}(\mathbf{m}_\lambda) + \alpha_2^\mu \Upsilon_{\text{TV}}(\mathbf{m}_\mu) + \alpha_2^\rho \Upsilon_{\text{TV}}(\mathbf{m}_\rho) \end{aligned} \quad (13)$$

The gradient for each parameter based on l1 norm:

$$\begin{pmatrix} \frac{\partial \Phi_{l_1}^{TV}}{\partial \mathbf{m}_\lambda} \\ \frac{\partial \Phi_{l_1}^{TV}}{\partial \mathbf{m}_\mu} \\ \frac{\partial \Phi_{l_1}^{TV}}{\partial \mathbf{m}_\rho} \end{pmatrix} = \begin{pmatrix} \mathbf{G}_{11_\lambda} \\ \mathbf{G}_{11_\mu} \\ \mathbf{G}_{11_\rho} \end{pmatrix} + \begin{pmatrix} \mathbf{R}_\lambda \\ \mathbf{R}_\mu \\ \mathbf{R}_\rho \end{pmatrix} \quad (14)$$

, where $\mathbf{G}_{11_\lambda}, \mathbf{G}_{11_\mu}, \mathbf{G}_{11_\rho}$ are the gradient for λ, μ, ρ using l_1 norm as misfit function. The gradient calculation in l_1 norm is using a differenta adjoint source (Pyun et al. (2009) Brossier et al. (2010)). The adjoint source for the adjoint fields for l_1 norm is , In the case of real arithmetic numbers, the term $\frac{\Delta \mathbf{d}}{|\Delta \mathbf{d}|}$ corresponds to the function *sign*. In this study, we did not meet conditions when $\Delta \mathbf{d} = 0$. The detail gradient expression using the adjoint state method for parameters λ, μ and ρ based on l_2 and l_1 norm can be expressed as:

$$\begin{aligned} \mathbf{G}_{12_\lambda} = & - \sum_{\mathbf{x}_s} \sum_{\mathbf{x}_g} \int_0^T \\ & ((\partial_x \tilde{u}_x(\mathbf{r}, \mathbf{r}_s, t) + \partial_z \tilde{u}_z(\mathbf{r}, \mathbf{r}_s, t)) (\partial_x \tilde{u}_x^{*l_2}(\mathbf{r}, \mathbf{r}_g, T-t) + \partial_z \tilde{u}_z^{*l_2}(\mathbf{r}, \mathbf{r}_g, T-t))) \end{aligned} \quad (15)$$

$$\begin{aligned} \mathbf{G}_{12_\mu} = & - \sum_{\mathbf{x}_s} \sum_{\mathbf{x}_g} \int_0^T \\ & ((\partial_x \tilde{u}_x(\mathbf{r}, \mathbf{r}_s, t) + \partial_x \tilde{u}_z(\mathbf{r}, \mathbf{r}_s, t)) (\partial_z \tilde{u}_x^{*l_2}(\mathbf{r}, \mathbf{r}_g, T-t) + \partial_x \tilde{u}_z^{*l_2}(\mathbf{r}, \mathbf{r}_g, T-t))) \\ & - 2((\partial_x \tilde{u}_x(\mathbf{r}, \mathbf{r}_s, t) \partial_x \tilde{u}_x^{*l_2}(\mathbf{r}, \mathbf{r}_g, T-t) + \partial_z \tilde{u}_z(\mathbf{r}, \mathbf{r}_s, t) \partial_z \tilde{u}_z^{*l_2}(\mathbf{r}, \mathbf{r}_g, T-t))) \end{aligned} \quad (16)$$

$$\mathbf{G}_{12_\rho} = \sum_{\mathbf{x}_s} \sum_{\mathbf{x}_g} \int_0^T ((\partial_t \tilde{u}_x(\mathbf{r}, \mathbf{r}_s, t) \partial_t \tilde{u}_x^{*l_2}(\mathbf{r}, \mathbf{r}_g, T-t) + \partial_t \tilde{u}_z(\mathbf{r}, \mathbf{r}_s, t) \partial_t \tilde{u}_z^{*l_2}(\mathbf{r}, \mathbf{r}_g, T-t))) \quad (17)$$

$$\begin{aligned} \mathbf{G}_{11_\lambda} = & - \sum_{\mathbf{x}_s} \sum_{\mathbf{x}_g} \int_0^T \\ & ((\partial_x \tilde{u}_x(\mathbf{r}, \mathbf{r}_s, t) + \partial_z \tilde{u}_z(\mathbf{r}, \mathbf{r}_s, t)) (\partial_x \tilde{u}_x^{*l_1}(\mathbf{r}, \mathbf{r}_g, T-t) + \partial_z \tilde{u}_z^{*l_1}(\mathbf{r}, \mathbf{r}_g, T-t))) \end{aligned} \quad (18)$$

$$\begin{aligned}
\mathbf{G}_{11\mu} = & - \sum_{\mathbf{x}_s} \sum_{\mathbf{x}_g} \int_0^T \\
& ((\partial_z \tilde{u}_x(\mathbf{r}, \mathbf{r}_s, t) + \partial_x \tilde{u}_z(\mathbf{r}, \mathbf{r}_s, t)) (\partial_z \tilde{u}_x^{*l1}(\mathbf{r}, \mathbf{r}_g, T-t) + \partial_x \tilde{u}_z^{*l1}(\mathbf{r}, \mathbf{r}_g, T-t))) \\
& - 2((\partial_x \tilde{u}_x(\mathbf{r}, \mathbf{r}_s, t) \partial_x \tilde{u}_x^{*l1}(\mathbf{r}, \mathbf{r}_g, T-t) + \partial_z \tilde{u}_z(\mathbf{r}, \mathbf{r}_s, t) \partial_z \tilde{u}_z^{*l1}(\mathbf{r}, \mathbf{r}_g, T-t)))
\end{aligned} \tag{19}$$

$$\mathbf{G}_{11\rho} = \sum_{\mathbf{x}_s} \sum_{\mathbf{x}_g} \int_0^T ((\partial_t \tilde{u}_x(\mathbf{r}, \mathbf{r}_s, t) \partial_t \tilde{u}_x^{*l1}(\mathbf{r}, \mathbf{r}_g, T-t) + \partial_t \tilde{u}_z(\mathbf{r}, \mathbf{r}_s, t) \partial_t \tilde{u}_z^{*l1}(\mathbf{r}, \mathbf{r}_g, T-t))) \tag{20}$$

$\mathbf{G}_{12\lambda}$, $\mathbf{G}_{12\mu}$, $\mathbf{G}_{12\rho}$, are gradients for λ , μ and ρ using l_2 norm as misfit respectively. $\mathbf{G}_{11\lambda}$, $\mathbf{G}_{11\mu}$, $\mathbf{G}_{11\rho}$, are gradients for λ , μ and ρ using l_1 norm as misfit respectively. \tilde{u}_x^{*l1} and \tilde{u}_z^{*l1} are the adjoint wavefields generated by the l_1 norm adjoint source, \tilde{u}_x^{*l2} and \tilde{u}_z^{*l2} are the adjoint wavefields generated by the l_2 norm adjoint source. T is the total receiving time for the shot records. \mathbf{r}_s , \mathbf{r}_g represent the source and receivers locations respectively. \mathbf{r} represent the model perturbation locations for λ , μ and ρ model. Figure 5 shows the gradient calculated using the adjoint state method and the Automatic Difference method. Figure 5 (a), (b), (c) are the normalized λ , μ and ρ gradients calculated by using the adjoint state method. Figure 5 (d), (e), (f) are the normalized λ , μ and ρ gradients calculated by using the Automatic Differential method. The gradients calculated by using the Automatic Difference method, contains more information about the model, for instance the lower part of the model, indicating that they can better reconstruct the mode. Now we rewrite the misfit function as:

$$\Phi^{TV} = \mathbf{J}_D + \mathbf{J}_{r1} + \mathbf{J}_{r2} \tag{21}$$

,where \mathbf{J}_D represents the any kind of norm misfit between observed data and synthetic data. $\mathbf{J}_{r1} = \alpha_1^\lambda \Theta_{TV}(\mathbf{m}_\lambda) + \alpha_1^\mu \Theta_{TV}(\mathbf{m}_\mu) + \alpha_1^\rho \Theta_{TV}(\mathbf{m}_\rho)$. $\mathbf{J}_{r2} = \alpha_2^\lambda \Upsilon_{TV}(\mathbf{m}_\lambda) + \alpha_2^\mu \Upsilon_{TV}(\mathbf{m}_\mu) + \alpha_2^\rho \Upsilon_{TV}(\mathbf{m}_\rho)$. The value α_1^λ , α_1^μ , α_1^ρ , α_2^λ , α_2^μ , α_2^ρ . are chosen according to the following

formula (Guitton et al. (2012)).

$$T = \frac{\mathbf{J}_D}{\mathbf{J}_{r1} + \mathbf{J}_{r2}} \quad (22)$$

We should control the values for α_1^λ , α_1^μ , α_1^ρ , α_2^λ , α_2^μ , α_2^ρ and keep value T between 1 and 10. T should be relatively large when, noise occurs in the data (Xiang and Zhang (2016)).

[Figure 5 about here.]

Parameterization testing

By modifying the RNN cells, and changing the trainable parameters, we can examine the influence of parameterization on waveform inversion within the deep learning formulation. Three sets of parameter classes are considered: the velocity parameterization (D-V model), involving P-wave velocity, S-wave velocity, and density; the modulus parameterization (D-M model), involving the Lamé parameters λ and μ , and density; and, the stiffness matrix model (D-S model), involving C_{11} , C_{44} and density ρ .

In these tests, the size of each model is 40×90 . 7 source points are evenly distributed across the surface of the model; the source is a Ricker wavelet with a dominant frequency of $30Hz$. The grid length of the model is $dx = dz = 4m$. In Figure 6 (a)-(b) are true and initial V_P model, (c)-(d) are the true and initial V_S model, (e)-(f) are the true and initial ρ model we use in this test.

In Figures 7 are the inversion results using the D-V parameterization. Figure 7 (a)-(d) are the inversion results for V_P generated by l_2 , l_2^{TV} , l_1 and l_1^{TV} norm. Figure 7 (e)-(h) are the inversion results for V_S generated by l_2 , l_2^{TV} , l_1 and l_1^{TV} norm. Figure 7 (i)-(l) are the inversion results for ρ generated by l_2 , l_2^{TV} , l_1 and l_1^{TV} norm. In Figure 7 (a), (e) and (i) we can see the cross talk between different parameters as the back arrows indicate, In Figure 7

(b), (c), (d) we can see that by changing the misfits and adding high order TV regulations, the cross talk between V_P and ρ has been reduced. In Figure 7 (h) and (l) we can see that by using l_1^{TV} norm, the cross talk between density and V_S has been mitigated, while in (j) and (k) we still see the cross talk between V_S and density. From Figures 7 we can see that l_1 norm with high order TV regulation can help to mitigate the cross talk problem.

[Figure 6 about here.]

[Figure 7 about here.]

Next the modulus parameterization is examined, in which we seek to recover λ , μ and ρ models. This occurs through a straightforward modification of the RNN cell, and again a change in the trainable parameters from velocities to moduli. Figure 8 (a)-(d) are the inversion results for λ generated by l_2 , l_2^{TV} , l_1 and l_1^{TV} norm. Figure 8 (e)-(h) are the inversion results for μ generated by l_2 , l_2^{TV} , l_1 and l_1^{TV} norm. Figure 8 (i)-(l) are the inversion results for ρ generated by l_2 , l_2^{TV} , l_1 and l_1^{TV} norm. In Figure 8 (b) and (d) we can see that by using the high order TV regulations in l_2 and l_1 norm the cross talk between density and λ has been mitigated. Figure (j) shows that In this parameterization by using the high order TV regulation on l_2 norm can provide better inversion results for density as well.

[Figure 8 about here.]

Inversion results for models in the S-D parameterization are plotted in Figure 9, generated using the change of variables $C_{11} = V_P^2 \rho$ and $C_{44} = V_S^2 \rho$. Figure 9 (a)-(d) are the inversion results for λ generated by l_2 , l_2^{TV} , l_1 and l_1^{TV} norm. Figure 9 (e)-(h) are the inversion results for μ generated by l_2 , l_2^{TV} , l_1 and l_1^{TV} norm. Figure 9 (i)-(l) are the inversion

results for ρ generated by l_2 , l_2^{TV} , l_1 and l_1^{TV} norm. In Figure 9 we can still see the cross talk between $c44$ and $c11$ as the black arrows pointing out. However this cross talk has been mitigated by in figure (d), by using the l_1^{TV} norm misfit. The inversion results above shows that the RNN based high order TV regulation FWI based on the l_2 and l_1 norm has the ability to mitigate cross talk problem with only gradient based methods. The RNN based l_2^{TV} RNN FWI in D-M parameterization and l_1^{TV} RNN FWI in D-S parameterization provide better inversion results than other inversion tests.

[Figure 9 about here.]

[Figure 10 about here.]

[Figure 11 about here.]

[Figure 12 about here.]

[Figure 13 about here.]

Next, we will verify the proposed methods on the over-thrust model. Figure 10 (a), (c), (e) demonstrate the true models for V_P , V_S , and density ρ model, and (b), (d) and (h) are the initial models for V_P , V_S , and density ρ respectively. The size of the model is 121×240 . The grid length of the model is 10m. 12 shots are evenly distributed on the surface of the model and every grid point has a receiver. The source of the wavelet is Ricker's wavelet with main frequency 20Hz.

Figure Figure 11 shows the inversion results by using the conventional FWI. Figure Figure 11 (a) is the inversion for V_P , Figure Figure 11 (b) is the inversion for V_S , Figure

Figure 11 (c) is the inversion for ρ . From figure 11 we can see that the overall inversion resolution by using the conventional FWI is poor.

Figure 12 shows the inversion results by using D-M parameterization. Figure 12 (a)-(c) are λ l_2 norm, l_2^{TV} norm, l_1^{TV} norm inversion results respectively, (d)-(f) are μ l_2 norm, l_2^{TV} norm, l_1^{TV} norm, inversion results respectively, (g)-(i) are ρ l_2 norm l_2^{TV} norm, l_1^{TV} norm inversion results respectively. In this parameterization we get unstable inversion results for parameter λ . However, in D-M parameterization Figure 13 (f), the small half arc structure at around 1000m of the model has been recovered in , as the black arrows indicate. Figure 13 shows the profiles through the recovered elastic modules at 1000m of the models based on D-M parameterization. In Figure 13, the black lines are the true values, the yellow lines are the initial values, red lines are the inversion results for l_2 norm, green lines are the inversion results for l_2^{TV} norm and blue lines are the inversion results for l_1^{TV} norm. Compared with the true lines we can also see that , Figure 13 (b) and Figure 13 (c), l_1^{TV} norm inversion results are more close to the true values.

[Figure 14 about here.]

[Figure 15 about here.]

[Figure 16 about here.]

Figure 14 shows the inversion results by using D-V parameterization. In this parameterization all the three parameters are stable. Figure 14 (a)-(c) are, V_P l_2 norm, l_2^{TV} norm, l_1^{TV} norm inversion results respectively, (d)-(f) are V_S l_2 norm, l_2^{TV} norm, l_1^{TV} norm, inversion results respectively, (g)-(i) are ρ l_2 norm l_2^{TV} norm, l_1^{TV} norm inversion results respectively. Compared with the true models ,we can see that the inversion results generated by using the

l_2 norm are less robust compared with other misfits. l_1 norm with high order TV regulation can provide more accurate inversion results. This can also be seen from Figure 14, which is the profiles through the recovered elastic modules at 1000m of the models. In Figure 14, the black lines are the true velocities and density, the yellow lines are the initial values, red lines are the inversion results for l_2 norm, green lines are the inversion results for l_2^{TV} norm and blue lines are the inversion results for l_1^{TV} norm. Figure 15 (a) shows the results for V_P . Figure 15 (b) shows the results for V_S . Figure 15 (c) shows the results for ρ . In all the three figures we can see that blue lines are closer to the true values compared with other lines, which means that the l_1^{TV} norm can provide us with more accurate inversion results. Figure 16 shows the D-V parameterization inversion model misfits in each iteration. The red lines are the inversion using l_2 norm. The green lines are the inversion using l_2^{TV} norm. The red lines are the inversion using l_1^{TV} norm. Figure 16 shows that we can get higher accuracy inversion results by using the l_1^{TV} norm with fewer iterations.

Figure 17 shows the inversion results by using D-S parameterization. Figure 17 (a)-(c), are c_{11} l_2 norm, l_2^{TV} norm, l_1^{TV} norm inversion results respectively, (d)-(f) are c_{44} l_2 norm, l_2^{TV} norm, l_1^{TV} norm, inversion results respectively, (g)-(i) are ρ l_2 norm l_2^{TV} norm, l_1^{TV} norm inversion results respectively. In this parameterization the small half arc structure at around 1000m of the model is clearly resolved in this parameterization by using the l_1^{TV} norm. Compared with other misfits, again the l_1^{TV} norm provide us the best resolution for the model. Figure 13 shows the profiles through the recovered elastic modules at 1000m of the models based on D-M parameterization. Red lines, green lines and blue lines are l_2 , l_2^{TV} , and l_1^{TV} norm inversion results respectively. We can also see that in D-S parameteriation, l_1^{TV} provide us with inversion results that is more close the to true values. Figure 18 shows how model misfits in D-M parameterization changes in each iteration. The blue line, the

l_1^{TV} norm inversion, has the fastest model misfit decline rate. We can conclude in this parameterization l_1^{TV} can generate more accuracy inversion results with fewer iterations.

[Figure 17 about here.]

[Figure 18 about here.]

[Figure 19 about here.]

RANDOM NOISE TESTING

In this section, we will test the sensitivity of this deep learning method to data contaminated with random noise drawn from a Gaussian distribution. In Figure 20, we plot a trace from an example shot profile with different ratios of noise.

[Figure 20 about here.]

In (a), the red signal is the record without noise, and the blue line is the record with Gaussian random noise. The mean value of the noise is zero, and the standard deviation is 0.3 ($std = 0.3$); in (b) the noise-free data and data with noise at $std = 0.5$ are plotted; in (c) the noise-free data and the data with noise at $std = 1$ are plotted.

[Figure 21 about here.]

In Figure 21a, e and i the inversion results from noise-free inversion based on the RNN are plotted. In Figure 21b, f and j, the inversion results with noise at $std = 0.3$ for V_P , V_S , and ρ are plotted, respectively; in Figure 21c, g, and k, the inversion results with noise at $std = 0.5$ for V_P , V_S , and ρ are plotted; in Figure 21d, h, and l are likewise for $std = 1.0$. We

conclude that a moderate amount of random error in the data used for the RNN training leads to acceptable results, though some blurring is introduced and detail in the structure is lost. The V_S recovery appears to be much more sensitive to noise than are those of V_P or ρ .

CONCLUSIONS

Elastic multi-parameter full waveform inversion can be formulated as a strongly constrained, theory-based deep-learning network. Specifically, a recurrent neural network, set up with rules enforcing elastic wave propagation, with the wavefield projected onto a measurement surface acting as the labeled data to be compared with observed seismic data, recapitulates elastic FWI but with both (1) the opportunity for data-driven learning to be incorporated, and (2) a design supported by powerful cloud computing architectures. Each cell of the recurrent neural network is designed according to the isotropic-elastic wave equation.

The partial derivatives of the data residual with respect to the trainable parameters which act to represent the elastic media are calculated by using the intelligent automatic differential method. With the automatic differential method, gradients can be automatically calculated via the chain rule, guided by backpropagation along the paths within the computational graph. The automatic differential method produces a high level of computational efficiency and scalability for the calculation of gradients for different parameters in elastic media. The formulation is suitable for exploring numerical features of different misfits and different parameterizations, with an aim of improving the resolution of the recovered elastic models, and mitigate cross-talk.

We compared RNN waveform inversions based on l_2 , l_1 with high order total variations.

We used this RNN synthetic environment to compare density-velocity (P-wave velocity, S-wave velocity, and density), modulus-density (Lamé parameters and density) and S-D (C_{11} , C_{44} and density) parameterizations, and their exposure to cross-talk for the varying misfit functions. Our results suggest generally that this approach to full waveform inversion is consistent and stable. S-D $l1$ norm with high order TV regulation can better resolve the elastic synthetic models. $l1$ norm with high order TV regulation can mitigate the cross-talk between parameters with gradient-based method.

REFERENCES

- Alkhalifah, T., and R.-É. Plessix, 2014, A recipe for practical full-waveform inversion in anisotropic media: An analytical parameter resolution study: *Geophysics*, **79**, R91–R101.
- Bar-Sinai, Y., S. Hoyer, J. Hickey, and M. P. Brenner, 2019, Learning data-driven discretizations for partial differential equations: *Proceedings of the National Academy of Sciences*, **116**, 15344–15349.
- Brossier, R., S. Operto, and J. Virieux, 2010, Which data residual norm for robust elastic frequency-domain full waveform inversion?: *Geophysics*, **75**, R37–R46.
- Chen, Y., M. Zhang, M. Bai, and W. Chen, 2019, Improving the signal-to-noise ratio of seismological datasets by unsupervised machine learning: *Seismological Research Letters*.
- Downton, J. E., and D. P. Hampson, 2018, Deep neural networks to predict reservoir properties from seismic: *CSEG Geoconvention*.
- Graves, A., A.-r. Mohamed, and G. Hinton, 2013, Speech recognition with deep recurrent neural networks: 2013 IEEE international conference on acoustics, speech and signal processing, *IEEE*, 6645–6649.
- Guitton, A., G. Ayeni, and E. Díaz, 2012, Constrained full-waveform inversion by model reparameterization geologically constrained fwi: *Geophysics*, **77**, R117–R127.
- Hughes, T. W., I. A. Williamson, M. Minkov, and S. Fan, 2019, Wave physics as an analog recurrent neural network: *Science Advances*, **5**, eaay6946.
- Innanen, K. A., 2014, Seismic avo and the inverse hessian in precritical reflection full waveform inversion: *Geophysical Journal International*, **199**, 717–734.
- Jin, G., K. Mendoza, B. Roy, and D. G. Buswell, 2019, Machine learning-based fracture-hit detection algorithm using lfdas signal: *The Leading Edge*, **38**, 520–524.
- Kalchbrenner, N., and P. Blunsom, 2013, Recurrent continuous translation models: 1700–

1709.

- Kamath, N., R. Brossier, L. Métivier, and P. Yang, 2018, 3d acoustic/visco-acoustic time-domain fwi of obc data from the valhall field, *in* SEG Technical Program Expanded Abstracts 2018: Society of Exploration Geophysicists, 1093–1097.
- Kamei, R., and R. Pratt, 2013, Inversion strategies for visco-acoustic waveform inversion: *Geophysical Journal International*, **194**, 859–884.
- Karpatne, A., G. Atluri, J. H. Faghmous, M. Steinbach, A. Banerjee, A. Ganguly, S. Shekhar, N. Samatova, and V. Kumar, 2017, Theory-guided data science: A new paradigm for scientific discovery from data: *IEEE Transactions on Knowledge and Data Engineering*, **29**, 2318–2331.
- Keating, S., and K. A. Innanen, 2017, Crosstalk and frequency bands in truncated newton an-acoustic full-waveform inversion: 1416–1421.
- , 2019, Parameter crosstalk and modeling errors in viscoacoustic seismic full-waveform inversion: *Geophysics*, **84**, R641–R653.
- Köhn, D., D. De Nil, A. Kurzman, A. Przebindowska, and T. Bohlen, 2012, On the influence of model parametrization in elastic full waveform tomography: *Geophysical Journal International*, **191**, 325–345.
- Lailly, P., 1983, as a sequence of before stack migrations: *Conference on Inverse Scattering—Theory and Application*, Siam, 206.
- Li, C., Y. Zhang, and C. C. Mosher, 2019a, A hybrid learning-based framework for seismic denoising: *The Leading Edge*, **38**, 542–549.
- Li, D., K. Xu, J. M. Harris, and E. Darve, 2019b, Time-lapse full waveform inversion for subsurface flow problems with intelligent automatic differentiation: arXiv preprint arXiv:1912.07552.

- Liu, Y., and M. K. Sen, 2009, An implicit staggered-grid finite-difference method for seismic modelling: *Geophysical Journal International*, **179**, 459–474.
- Mikolov, T., 2012, Statistical language models based on neural networks: Master’s thesis.
- Oh, J.-W., and T. Alkhalifah, 2016, Elastic orthorhombic anisotropic parameter inversion: An analysis of parameterization elastic orthorhombic anisotropic fwi: *Geophysics*, **81**, C279–C293.
- Operto, S., Y. Gholami, V. Prioux, A. Ribodetti, R. Brossier, L. Metivier, and J. Virieux, 2013, A guided tour of multiparameter full-waveform inversion with multicomponent data: From theory to practice: *The leading edge*, **32**, 1040–1054.
- Pan, W., K. A. Innanen, and Y. Geng, 2018, Elastic full-waveform inversion and parametrization analysis applied to walk-away vertical seismic profile data for unconventional (heavy oil) reservoir characterization: *Geophysical Journal International*, **213**, 1934–1968.
- Pan, W., K. A. Innanen, G. F. Margrave, M. C. Fehler, X. Fang, and J. Li, 2016, Estimation of elastic constants for hti media using gauss-newton and full-newton multiparameter full-waveform inversion: *Geophysics*, **81**, R275–R291.
- Paszke, A., S. Gross, S. Chintala, G. Chanan, E. Yang, Z. DeVito, Z. Lin, A. Desmaison, L. Antiga, and A. Lerer, 2017, Automatic differentiation in pytorch.
- Peters, B., E. Haber, and J. Granek, 2019, Neural-networks for geophysicists and their application to seismic data interpretation: arXiv preprint arXiv:1903.11215.
- Plessix, R.-E., 2006, A review of the adjoint-state method for computing the gradient of a functional with geophysical applications: *Geophysical Journal International*, **167**, 495–503.
- Podlozhnyuk, V., 2007, Image convolution with cuda: NVIDIA Corporation white paper,

June, **2097**.

- Pyun, S., W. Son, and C. Shin, 2009, Frequency-domain waveform inversion using an l1-norm objective function: *Exploration Geophysics*, **40**, 227–232.
- Raissi, M., 2018, Deep hidden physics models: Deep learning of nonlinear partial differential equations: *The Journal of Machine Learning Research*, **19**, 932–955.
- Richardson, A., 2018, Seismic full-waveform inversion using deep learning tools and techniques: arXiv preprint arXiv:1801.07232.
- Röth, G., and A. Tarantola, 1994, Neural networks and inversion of seismic data: *Journal of Geophysical Research: Solid Earth*, **99**, 6753–6768.
- Sambridge, M., P. Rickwood, N. Rawlinson, and S. Sommacal, 2007, Automatic differentiation in geophysical inverse problems: *Geophysical Journal International*, **170**, 1–8.
- Shustak, M., and E. Landa, 2018, Time reversal for wave refocusing and scatterer detection using machine learning: *Geophysics*, **83**, T257–T263.
- Smith, R., T. Mukerji, and T. Lupo, 2019, Correlating geologic and seismic data with unconventional resource production curves using machine learning: *Geophysics*, **84**, O39–O47.
- Sun, H., and L. Demanet, 2018, Low frequency extrapolation with deep learning, *in* SEG Technical Program Expanded Abstracts 2018: Society of Exploration Geophysicists, 2011–2015.
- Sun, J., Z. Niu, K. A. Innanen, J. Li, and D. O. Trad, 2020, A theory-guided deep-learning formulation and optimization of seismic waveform inversion: *Geophysics*, **85**, R87–R99.
- Tarantola, A., 1984, Inversion of seismic reflection data in the acoustic approximation: *Geophysics*, **49**, 1259–1266.
- , 1986, A strategy for nonlinear elastic inversion of seismic reflection data: *Geophysics*,

- 51**, 1893–1903.
- Virieux, J., 1986, P-sv wave propagation in heterogeneous media: Velocity-stress finite-difference method: *Geophysics*, **51**, 889–901.
- Wagner, N., and J. M. Rondinelli, 2016, Theory-guided machine learning in materials science: *Frontiers in Materials*, **3**, 28.
- Wu, J.-L., H. Xiao, and E. Paterson, 2018, Physics-informed machine learning approach for augmenting turbulence models: A comprehensive framework: *Physical Review Fluids*, **3**, 074602.
- Wu, Y., and Y. Lin, 2018, Inversionnet: A real-time and accurate full waveform inversion with cnns and continuous crfs: arXiv preprint arXiv:1811.07875.
- Xiang, S., and H. Zhang, 2016, Efficient edge-guided full-waveform inversion by canny edge detection and bilateral filtering algorithms: *Geophysical Supplements to the Monthly Notices of the Royal Astronomical Society*, **207**, 1049–1061.
- Yang, F., and J. Ma, 2019, Deep-learning inversion: a next generation seismic velocity-model building method: *Geophysics*, **84**, 1–133.
- Zaremba, W., I. Sutskever, and O. Vinyals, 2014, Recurrent neural network regularization: arXiv preprint arXiv:1409.2329.
- Zhang, Z., Y. Wu, Z. Zhou, and Y. Lin, 2019, Velocitygan: Subsurface velocity image estimation using conditional adversarial networks: 2019 IEEE Winter Conference on Applications of Computer Vision (WACV), IEEE, 705–714.
- Zheng, Y., Q. Zhang, A. Yusifov, and Y. Shi, 2019, Applications of supervised deep learning for seismic interpretation and inversion: *The Leading Edge*, **38**, 526–533.

Algorithm 1 Sequence of calculations in the RNN cell with PML boundary

Require: Source: s_x, s_z ; velocity and stress fields at the previous time step, parameters

$:\lambda, \mu, \rho$; time step: dt . PML damping coefficients d_x, d_z .

Ensure: Update velocity field at $t + \frac{1}{2}$ and stress fields at $t + 1$

- 1: $\sigma_{xx}^t \leftarrow \sigma_{xx}^t + s_x$
- 2: $\sigma_{zz}^t \leftarrow \sigma_{zz}^t + s_z$
- 3: $\partial_x \sigma_{xx}^t \leftarrow (\sigma_{xx}^t * \mathbf{k}_{x1}) / \rho$
- 4: $\partial_z \sigma_{xz}^t \leftarrow (\sigma_{xz}^t * \mathbf{k}_{z2}) / \rho$
- 5: $\partial_x \sigma_{xz}^t \leftarrow (\sigma_{xz}^t * \mathbf{k}_{x2}) / \rho$
- 6: $\partial_z \sigma_{zz}^t \leftarrow (\sigma_{zz}^t * \mathbf{k}_{z1}) / \rho$
- 7: $v_x^{t+\frac{1}{2}} \leftarrow (1 - dt d_x) v_x^{t-\frac{1}{2}} + dt (\partial_x \sigma_{xx}^t)$
- 8: $v_x^{t+\frac{1}{2}} \leftarrow (1 - dt d_z) v_x^{t-\frac{1}{2}} + dt (\partial_z \sigma_{xz}^t)$
- 9: $v_x^{t+\frac{1}{2}} \leftarrow v_x^{t+\frac{1}{2}} + v_x^{t+\frac{1}{2}}$
- 10: $v_z^{t+\frac{1}{2}} \leftarrow (1 - dt d_x) v_z^{t-\frac{1}{2}} + dt (\partial_x \sigma_{xz}^t)$
- 11: $v_z^{t+\frac{1}{2}} \leftarrow (1 - dt d_z) v_z^{t-\frac{1}{2}} + dt (\partial_z \sigma_{zz}^t)$
- 12: $v_z^{t+\frac{1}{2}} \leftarrow v_z^{t+\frac{1}{2}} + v_z^{t+\frac{1}{2}}$
- 13: $\partial_x v_x^{t+\frac{1}{2}} \leftarrow v_x^{t+\frac{1}{2}} * \mathbf{k}_{x2}$
- 14: $\partial_z v_x^{t+\frac{1}{2}} \leftarrow v_x^{t+\frac{1}{2}} * \mathbf{k}_{z1}$
- 15: $\partial_x v_z^{t+\frac{1}{2}} \leftarrow v_z^{t+\frac{1}{2}} * \mathbf{k}_{x1}$
- 16: $\partial_z v_z^{t+\frac{1}{2}} \leftarrow v_z^{t+\frac{1}{2}} * \mathbf{k}_{z2}$
- 17: $\sigma_{xx}^{t+1} \leftarrow (1 - dt d_x) \sigma_{xx}^t + dt (\lambda + 2\mu) \partial_x v_x^{t+\frac{1}{2}}$
- 18: $\sigma_{zz}^{t+1} \leftarrow (1 - dt d_z) \sigma_{zz}^t + dt (\lambda) \partial_z v_z^{t+\frac{1}{2}}$
- 19: $\sigma_{zz}^{t+1} \leftarrow \sigma_{zz}^{t+1} + \sigma_{zz}^{t+1}$
- 20: $\sigma_{zx}^{t+1} \leftarrow (1 - dt d_x) \sigma_{zx}^t + dt (\lambda) \partial_x v_x^{t+\frac{1}{2}}$
- 21: $\sigma_{zz}^{t+1} \leftarrow (1 - dt d_z) \sigma_{zz}^t + dt (\lambda + 2\mu) \partial_z v_z^{t+\frac{1}{2}}$
- 22: $\sigma_{zz}^{t+1} \leftarrow \sigma_{zz}^{t+1} + \sigma_{zz}^{t+1}$
- 23: $\sigma_{xz}^{t+1} \leftarrow (1 - dt d_x) \sigma_{xz}^t + dt (\mu) \partial_x v_x^{t+\frac{1}{2}}$

Algorithm 2 Loop for elastic RNN FWI

- 1: Set trainable parameters: λ, μ, ρ in this test.
 - 2: Set optimizers for parameters: $Optimizer_1, Optimizer_2$ and $Optimizer_3$ for λ, μ and ρ respectively.
 - 3: **for** $iter \in [1, maxiter]$ or not converge **do**
 - 4: $D_{syn} = \text{RNN}(\lambda, \mu, \rho)$: generate synthetic data
 - 5: $loss = \text{costFunc}(D_{syn}, D_{obs})$: calculate misfits
 - 6: $loss.backward()$: Backpropagation and give gradients for the parameters
 - 7: $optimizers.step()$: update parameters
 - 8: **end for**
-

LIST OF FIGURES

- 1 Forward propagation through an example RNN. Cells are identical in form, with the output of one being the input of the next. $\mathbf{O} = [O_1, O_2, O_3, \dots]$ are the internal variables in each cell; $\mathbf{S} = [S_1, S_2]$ are the inputs; $\mathbf{P} = [P_1, P_2]$ are the outputs; $\mathbf{L} = [L_1, L_2]$ are the labeled data; $\mathbf{W} = [W_1, W_2]$ are the trainable weights. Black dashed line indicates forward propagation. 34
- 2 Residual backward propagation through an example RNN. $\mathbf{R} = [R_1, R_2]$ are the residuals at each RNN cell, which are calculated using absolute error (l_1 norm). Gray solid line shows how gradients are calculated using back propagation from the residual to the trainable weights in RNN cell along the computational graph. 35
- 3 The structure of each RNN. In this figure, $\partial_x \sigma_{xx}^t, \partial_z \sigma_{zz}^t, \partial_x \sigma_{xz}^t, \partial_z \sigma_{xz}^t, \partial_x v_x^{t+\frac{1}{2}}, \partial_z v_x^{t+\frac{1}{2}}, \partial_x v_z^{t+\frac{1}{2}}, \partial_z v_z^{t+\frac{1}{2}}$ are the internal variables. $v_x^{t-\frac{1}{2}}, v_z^{t-\frac{1}{2}}, \sigma_{xx}^t, \sigma_{zz}^t, \sigma_{xz}^t$ is communicated between the RNN cells. λ, μ, ρ are trainable parameters. 36
- 4 Velocity field forward and residual backward propagation under formatting of the RNN. The shot records formed at each time step correspond to the output of RNN cell P in Figure 2. Observed shot records correspond to labeled data (L in Figure 2). Residual shot record correspond to residual information (R in Figure 2). Back propagation starts from the residual shot record. 37
- 5 (a) λ gradient given by the adjoint state method. (b) μ gradient based by the adjoint state method. (c) ρ gradient based by the adjoint state method. (d) λ gradient given by the AD method. (e) μ gradient based by the AD method. (f) ρ gradient based by the AD method. 38
- 6 (a) true V_P model, (b) initial V_S model, (c) true V_S model, (d) initial vs model, (e) true ρ mode, (f) initial ρ model. 39
- 7 D-V parameterization inversion results. (a)-(d), V_P l_2 norm, l_2^{TV} norm, l_1 norm, l_1^{TV} norm inversion results respectively, (e)-(h), V_S l_2 norm, l_2^{TV} norm, l_1 norm, l_1^{TV} norm inversion results respectively, (i)-(l), ρ l_2 norm, l_2^{TV} norm, l_1 norm, l_1^{TV} norm inversion results respectively. 40
- 8 D-M parameterization inversion results. (a)-(d), λ l_2 norm, l_2^{TV} norm, l_1 norm, l_1^{TV} norm inversion results respectively, (e)-(h), μ l_2 norm, l_2^{TV} norm, l_1 norm, l_1^{TV} norm inversion results respectively, (i)-(l), ρ l_2 norm, l_2^{TV} norm, l_1 norm, l_1^{TV} norm inversion results respectively. 41
- 9 D-S parameterization inversion results. (a)-(d), c_{11} l_2 norm, l_2^{TV} norm, l_1 norm, l_1^{TV} norm inversion results respectively, (e)-(h), c_{44} l_2 norm, l_2^{TV} norm, l_1 norm, l_1^{TV} norm inversion results respectively, (i)-(l), ρ l_2 norm, l_2^{TV} norm, l_1 norm, l_1^{TV} norm inversion results respectively. 42
- 10 (a) true V_P model, (b) initial V_P model, (c) true V_S model (d) initial V_S model, (e) ρ true (f) initial ρ 43

11	(a) true V_P model, (b) initial V_P model, (c) true V_S model (d) initial V_S model, (e) ρ true (f) initial ρ	44
12	M-D parameterization inversion results. (a)-(c), λ l_2 norm, l_2^{TV} norm, l_1^{TV} norm inversion results respectively, (c)-(f), μ l_2 norm, l_2^{TV} norm, l_1^{TV} norm, inversion results respectively, (g)-(i), ρ l_2 norm l_2^{TV} norm, l_1^{TV} norm inversion results respectively	45
13	Profiles through the recovered elastic models. (a) Vertical λ profiles; (b) vertical μ profiles; (c) vertical ρ profiles	46
14	D-V parameterization inversion results. (a)-(d), V_P l_2 norm, l_2^{TV} norm, l_1^{TV} norm inversion results respectively, (e)-(h), V_S l_2 norm, l_2^{TV} norm, l_1^{TV} norm, inversion results respectively, (i)-(l), ρ l_2 norm l_2^{TV} norm, l_1^{TV} norm inversion results respectively.	47
15	Profiles through the recovered elastic models. (a) Vertical V_P profiles; (b) vertical V_S profiles; (c) vertical ρ profiles.	48
16	D-V parameterization inversion results . (a) V_p model misfit using l_2, l_2^{TV} and l_1^{TV} norm.(b) V_s model misfit using l_2, l_2^{TV} and l_1^{TV} norm.(c) ρ model misfit using l_2, l_2^{TV} and l_1^{TV} norm	49
17	S-D parameterization inversion results. (a)-(c), c_{11} l_2 norm, l_2^{TV} norm, l_1^{TV} norm inversion results respectively, (c)-(f), c_{44} l_2 norm, l_2^{TV} norm, l_1^{TV} norm, inversion results respectively, (g)-(i), ρ l_2 norm l_2^{TV} norm, l_1^{TV} norm inversion results respectively.	50
18	Profiles through the recovered elastic models based on . (a) Vertical c_{11} profiles; (b) vertical c_{44} profiles; (c) vertical ρ profiles	51
19	D-S parameterization inversion results . (a) c_{11} model misfit using l_2, l_2^{TV} and l_1^{TV} norm.(b) c_{44} model misfit using l_2, l_2^{TV} and l_1^{TV} norm.(c) ρ model misfit using l_2, l_2^{TV} and l_1^{TV} norm	52
20	Noise free and noise shotrecords. (a) Noise free record and records with Gaussian noise $std = 0.3$. (b) Noise free record and records with Gaussian noise $std = 0.5$. (c) Noise free record and records with Gaussian noise $std = 1$	53
21	Random noise testing inversion results. (a),(e),(i), noise free inversion results for V_P , V_S , and density (b),(f),(j) Gaussian noise $std = 0.3$ inversion results for V_P , V_S , and density, (c),(g),(k) Gaussian noise $std = 0.5$ inversion results for V_P , V_S , and density, (d),(h),(l) Gaussian noise $std = 1.0$ inversion results for V_P , V_S , and density.	54

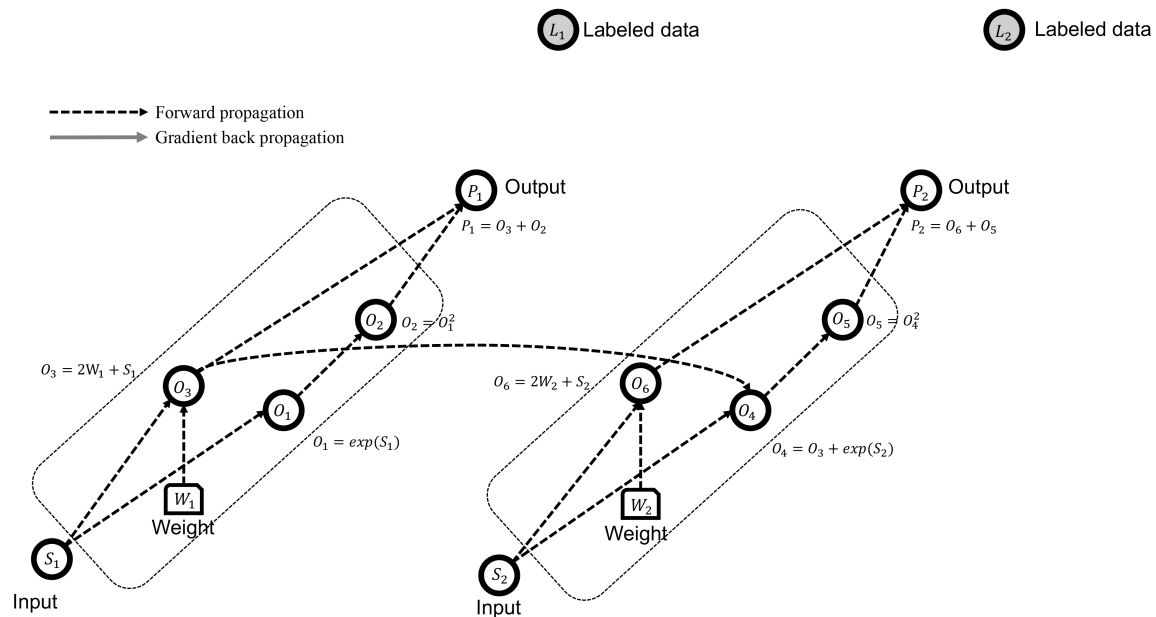


Figure 1: Forward propagation through an example RNN. Cells are identical in form, with the output of one being the input of the next. $\mathbf{O} = [O_1, O_2, O_3, \dots]$ are the internal variables in each cell; $\mathbf{S} = [S_1, S_2]$ are the inputs; $\mathbf{P} = [P_1, P_2]$ are the outputs; $\mathbf{L} = [L_1, L_2]$ are the labeled data; $\mathbf{W} = [W_1, W_2]$ are the trainable weights. Black dashed line indicates forward propagation.

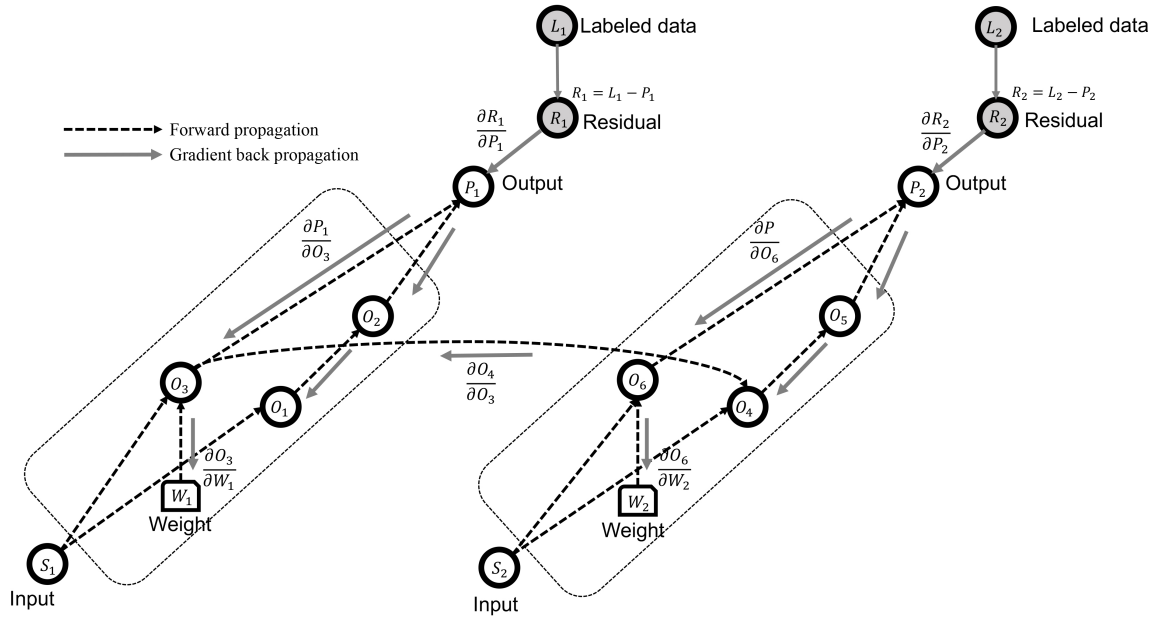


Figure 2: Residual backward propagation through an example RNN. $\mathbf{R} = [R_1, R_2]$ are the residuals at each RNN cell, which are calculated using absolute error (l_1 norm). Gray solid line shows how gradients are calculated using back propagation from the residual to the trainable weights in RNN cell along the computational graph.

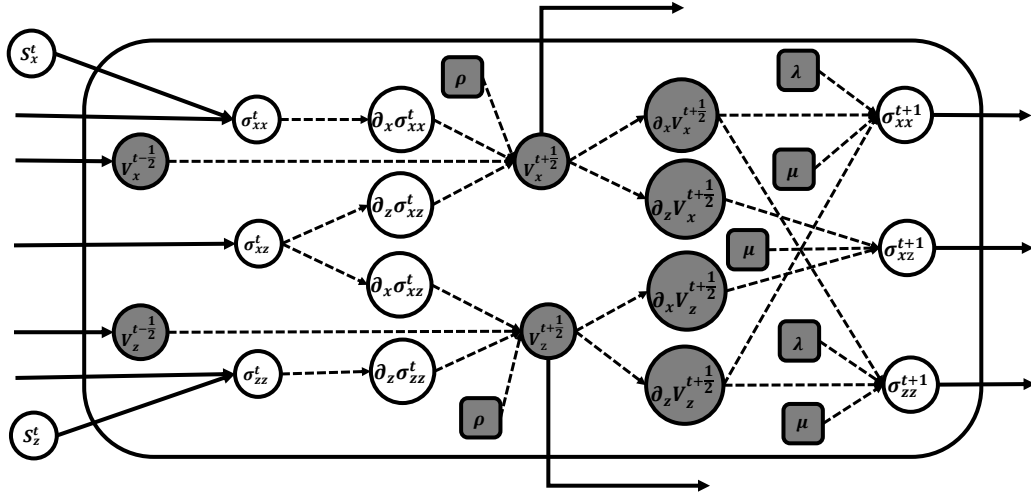


Figure 3: The structure of each RNN. In this figure, $\partial_x \sigma_{xx}^t$, $\partial_z \sigma_{zz}^t$, $\partial_x \sigma_{xz}^t$, $\partial_z \sigma_{xz}^t$, $\partial_x v_x^{t+\frac{1}{2}}$, $\partial_z v_x^{t+\frac{1}{2}}$, $\partial_x v_z^{t+\frac{1}{2}}$, $\partial_z v_z^{t+\frac{1}{2}}$ are the internal variables. $v_x^{t-\frac{1}{2}}$, $v_z^{t-\frac{1}{2}}$, σ_{xx}^t , σ_{zz}^t , σ_{xz}^t , is communicated between the RNN cells. λ , μ , ρ are trainable parameters.

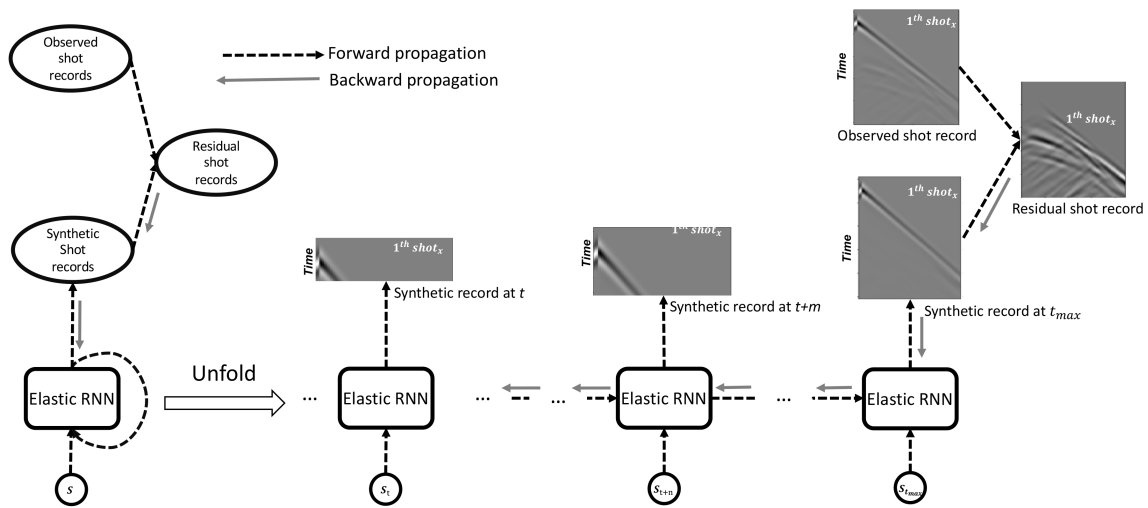


Figure 4: Velocity field forward and residual backward propagation under formatting of the RNN. The shot records formed at each time step correspond to the output of RNN cell P in Figure 2. Observed shot records correspond to labeled data (L in Figure 2). Residual shot record correspond to residual information (R in Figure 2). Back propagation starts from the residual shot record.

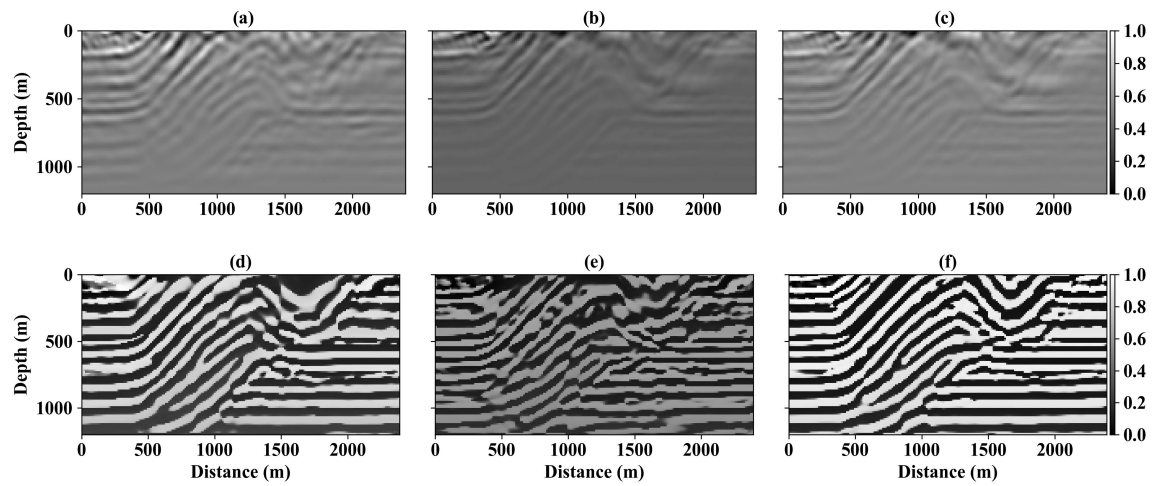


Figure 5: (a) λ gradient given by the adjoint state method. (b) μ gradient based by the adjoint state method. (c) ρ gradient based by the adjoint state method. (d) λ gradient given by the AD method. (e) μ gradient based by the AD method. (f) ρ gradient based by the AD method.

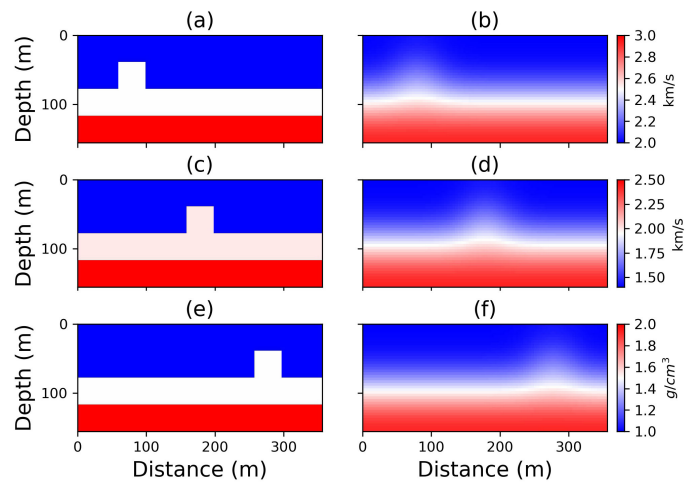


Figure 6: (a) true V_p model, (b) initial V_s model, (c) true V_s model, (d) initial v_s model, (e) true ρ model, (f) initial ρ model.

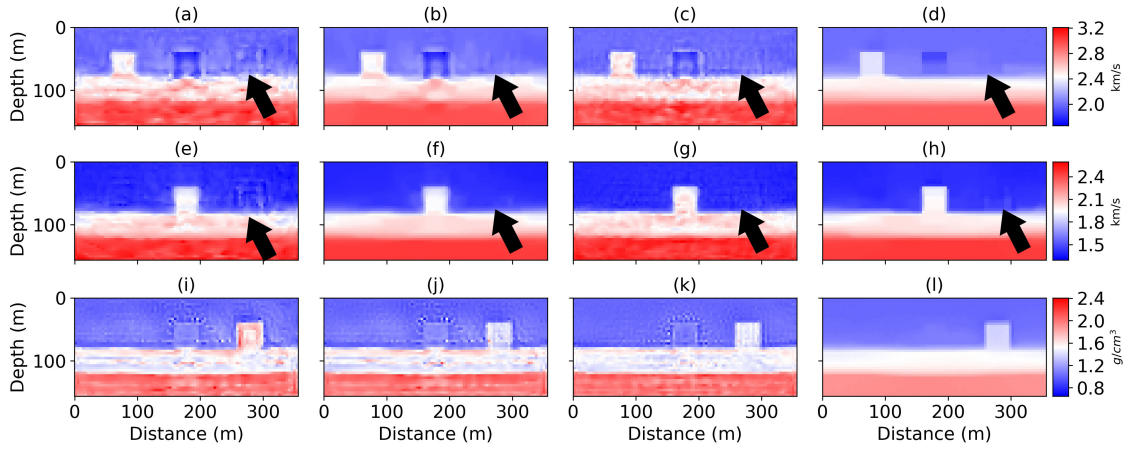


Figure 7: D-V parameterization inversion results. (a)-(d), V_P l_2 norm, l_2^{TV} norm, l_1 norm, l_1^{TV} norm inversion results respectively, (e)-(h), V_S l_2 norm, l_2^{TV} norm, l_1 norm, l_1^{TV} norm, inversion results respectively, (i)-(l), ρ l_2 norm, l_2^{TV} norm, l_1 norm, l_1^{TV} norm inversion results respectively.

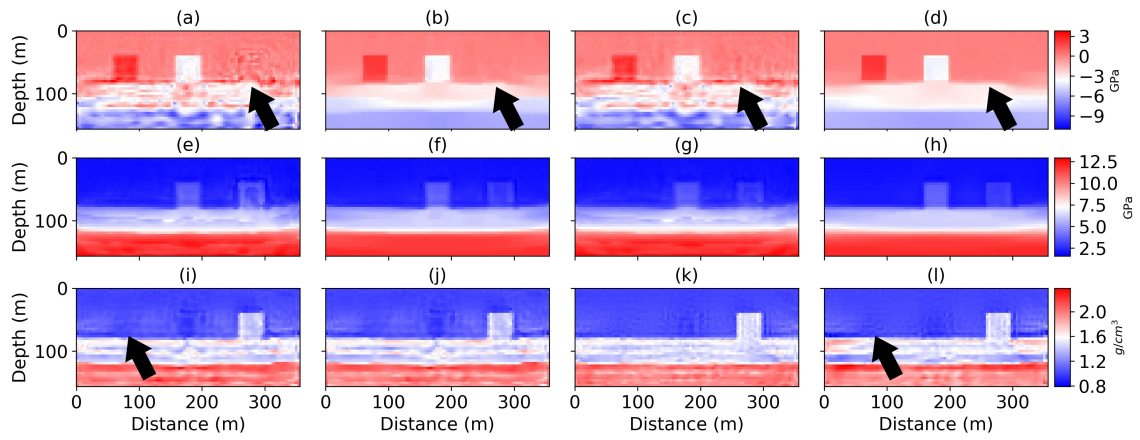


Figure 8: D-M parameterization inversion results. (a)-(d), λ l_2 norm, l_2^{TV} norm, l_1 norm, l_1^{TV} norm inversion results respectively, (e)-(h), μ l_2 norm, l_2^{TV} norm, l_1 norm, l_1^{TV} norm inversion results respectively, (i)-(l), ρ l_2 norm, l_2^{TV} norm, l_1 norm, l_1^{TV} norm inversion results respectively.

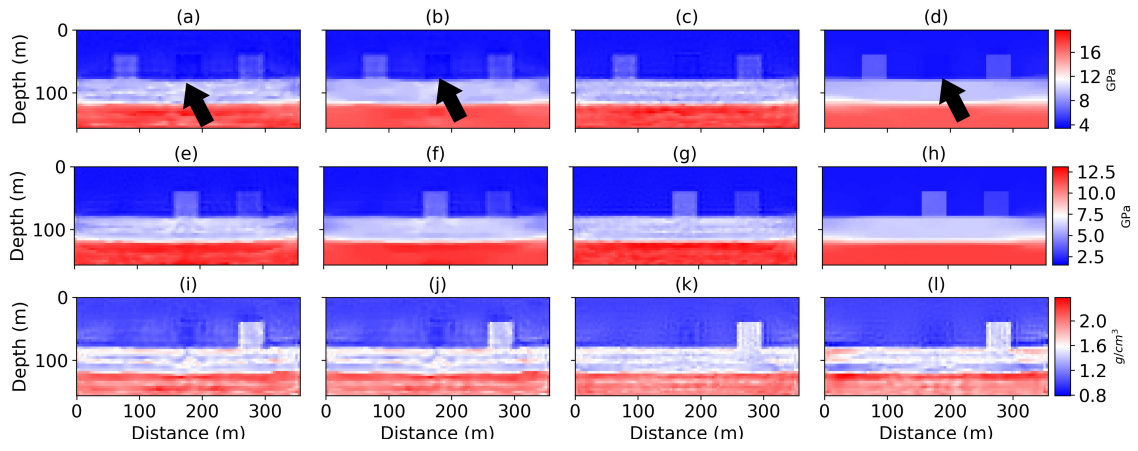


Figure 9: D-S parameterization inversion results. (a)-(d), c_{11} l_2 norm, l_2^{TV} norm, l_1 norm, l_1^{TV} norm inversion results respectively, (e)-(h), c_{44} l_2 norm, l_2^{TV} norm, l_1 norm l_1^{TV} norm, inversion results respectively, (i)-(l), ρ l_2 norm l_2^{TV} norm, l_1 norm, l_1^{TV} norm inversion results respectively.

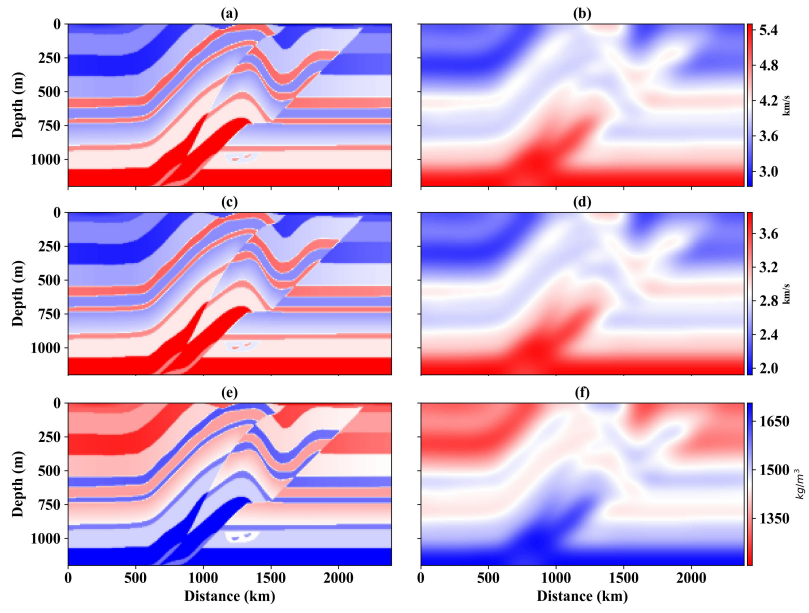


Figure 10: (a) true V_P model, (b) initial V_P model, (c) true V_S model (d) initial V_S model, (e) ρ true (f) initial ρ

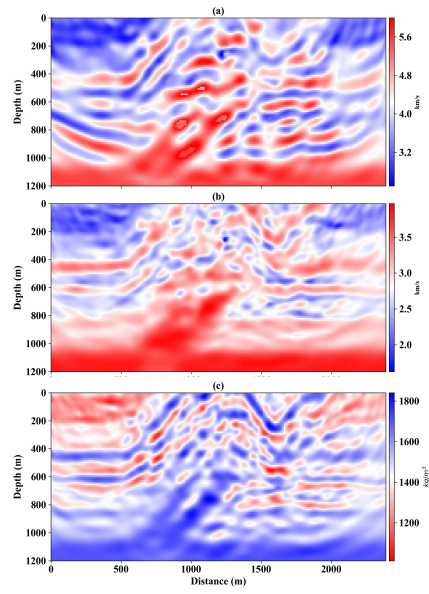


Figure 11: (a) true V_P model, (b) initial V_P model, (c) true V_S model (d) initial V_S model, (e) ρ true (f) initial ρ

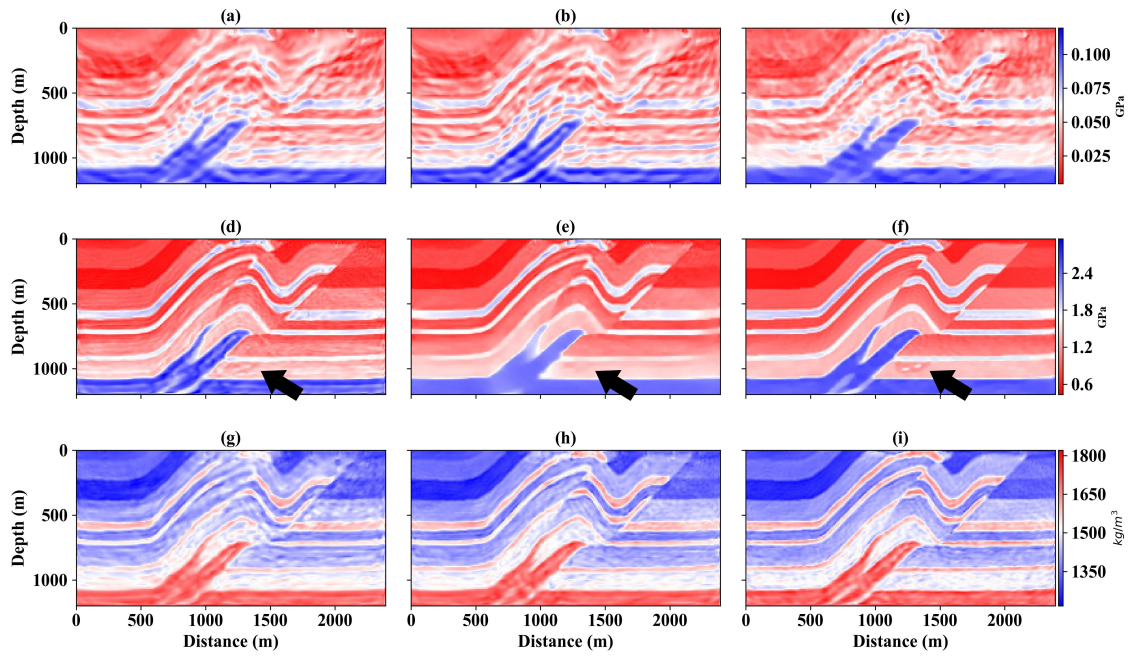


Figure 12: M-D parameterization inversion results. (a)-(c), λ l_2 norm, l_2^{TV} norm, l_1^{TV} norm inversion results respectively, (c)-(f), μ l_2 norm, l_2^{TV} norm, l_1^{TV} norm, inversion results respectively, (g)-(i), ρ l_2 norm l_2^{TV} norm, l_1^{TV} norm inversion results respectively

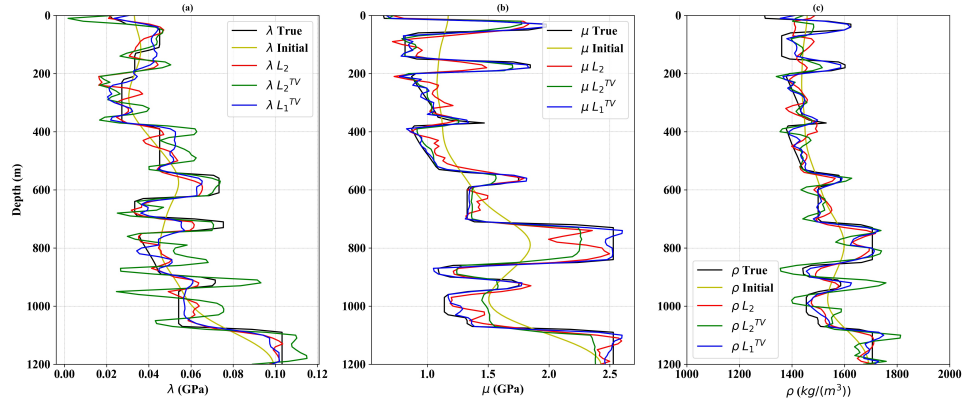


Figure 13: Profiles through the recovered elastic models. (a) Vertical λ profiles; (b) vertical μ profiles; (c) vertical ρ profiles

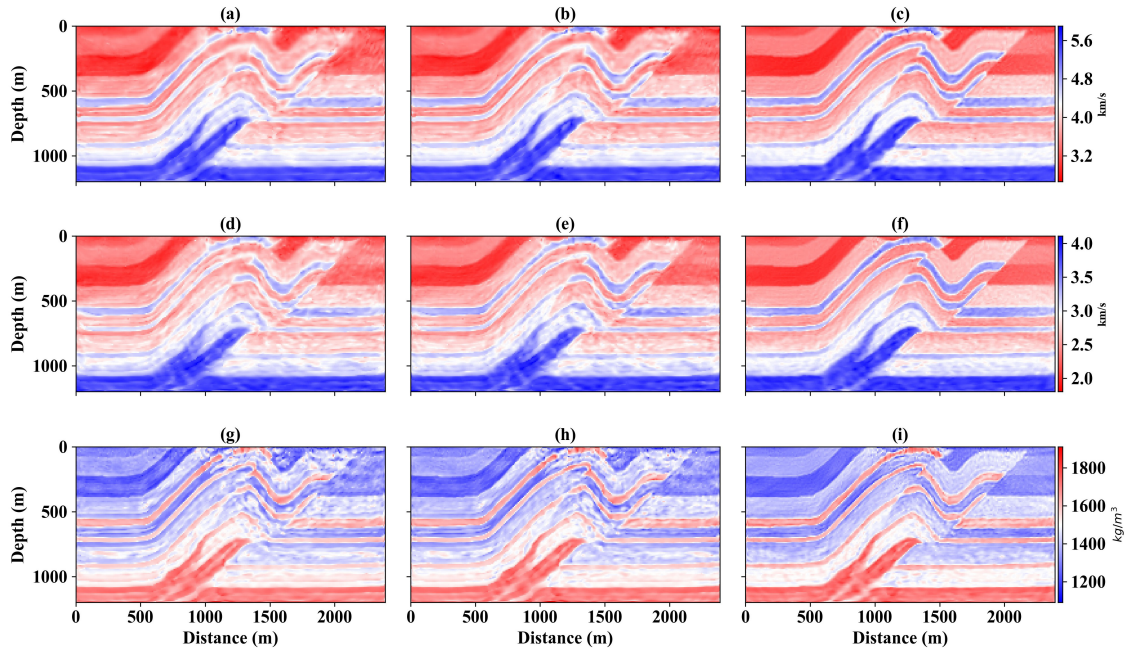


Figure 14: D-V parameterization inversion results. (a)-(d), V_P l_2 norm, l_2^{TV} norm, l_1^{TV} norm inversion results respectively, (e)-(h), V_S l_2 norm, l_2^{TV} norm, l_1^{TV} norm, inversion results respectively, (i)-(l), ρ l_2 norm, l_2^{TV} norm, l_1^{TV} norm inversion results respectively.

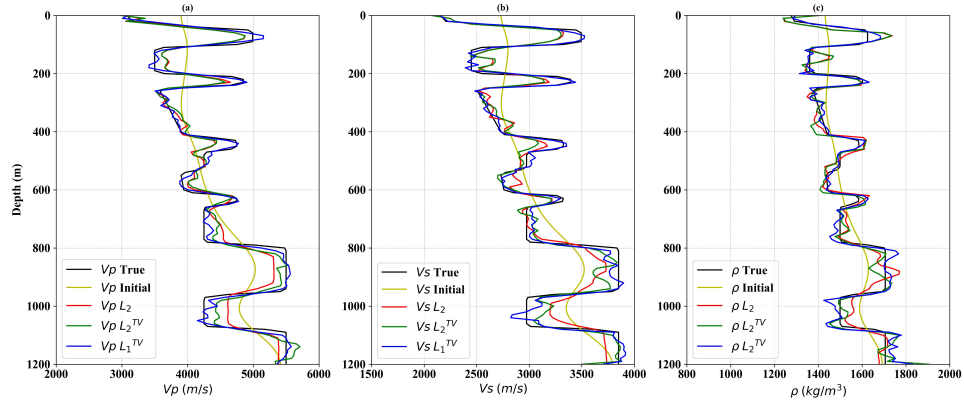


Figure 15: Profiles through the recovered elastic models. (a) Vertical V_P profiles; (b) vertical V_S profiles; (c) vertical ρ profiles.

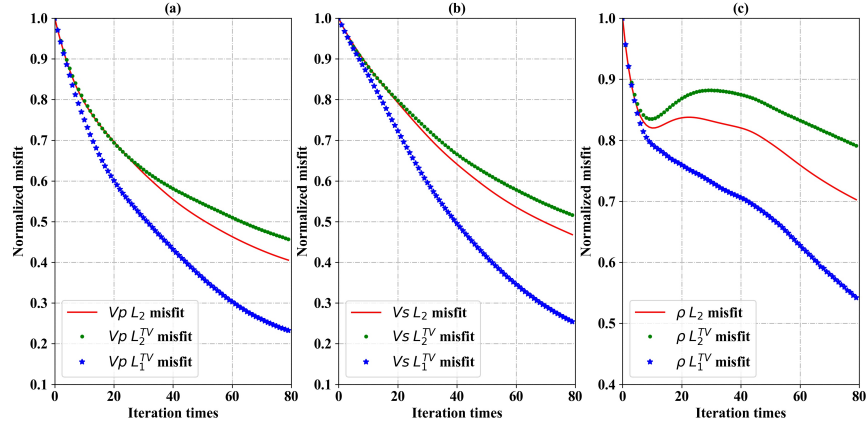


Figure 16: D-V parameterization inversion results . (a) Vp model misfit using l_2, l_2^{TV} and l_1^{TV} norm.(b) Vs model misfit using l_2, l_2^{TV} and l_1^{TV} norm.(c) ρ model misfit using l_2, l_2^{TV} and l_1^{TV} norm

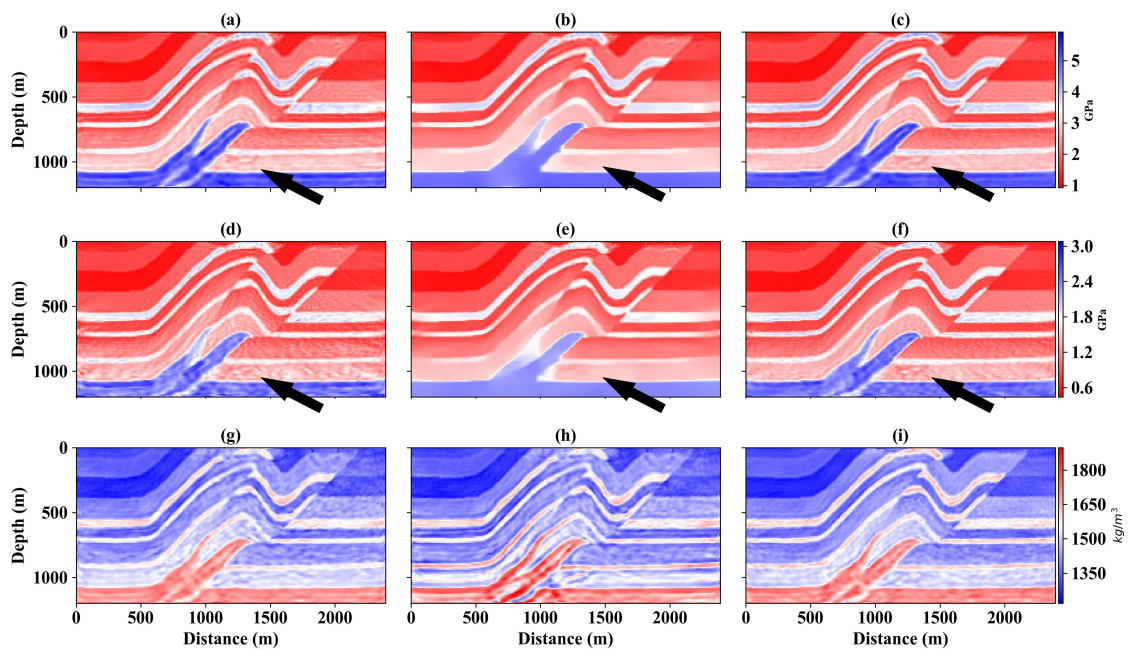


Figure 17: S-D parameterization inversion results. (a)-(c), c_{11} l_2 norm, l_2^{TV} norm, l_1^{TV} norm inversion results respectively, (d)-(f), c_{44} l_2 norm, l_2^{TV} norm, l_1^{TV} norm, inversion results respectively, (g)-(i), ρ l_2 norm l_2^{TV} norm, l_1^{TV} norm inversion results respectively.

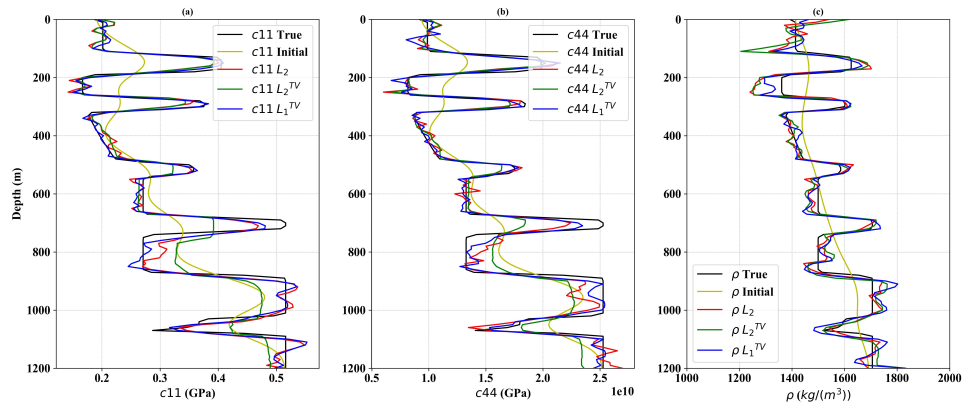


Figure 18: Profiles through the recovered elastic models based on . (a) Vertical c_{11} profiles; (b) vertical c_{44} profiles; (c) vertical ρ profiles

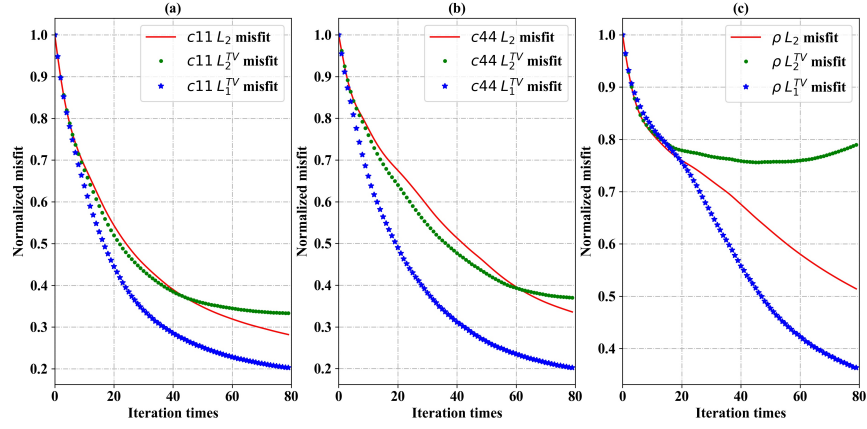


Figure 19: D-S parameterization inversion results . (a) $c11$ model misfit using l_2, l_2^{TV} and l_1^{TV} norm.(b) $c44$ model misfit using l_2, l_2^{TV} and l_1^{TV} norm.(c) ρ model misfit using l_2, l_2^{TV} and l_1^{TV} norm

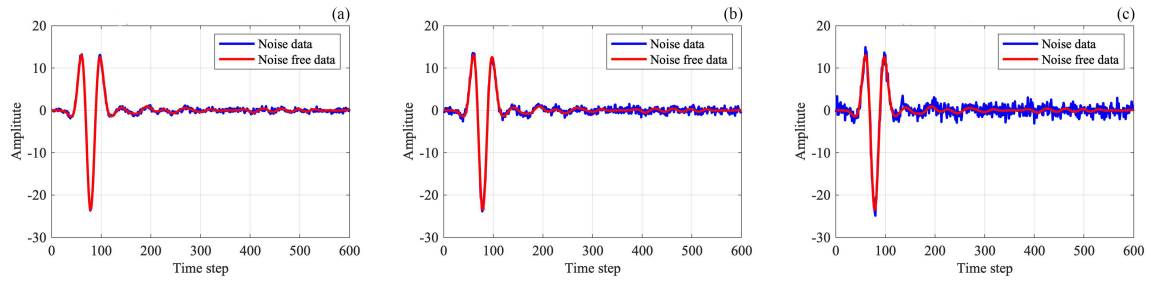


Figure 20: Noise free and noise shotrecords. (a) Noise free record and records with Gaussian noise $std = 0.3$. (b) Noise free record and records with Gaussian noise $std = 0.5$. (c) Noise free record and records with Gaussian noise $std = 1$.

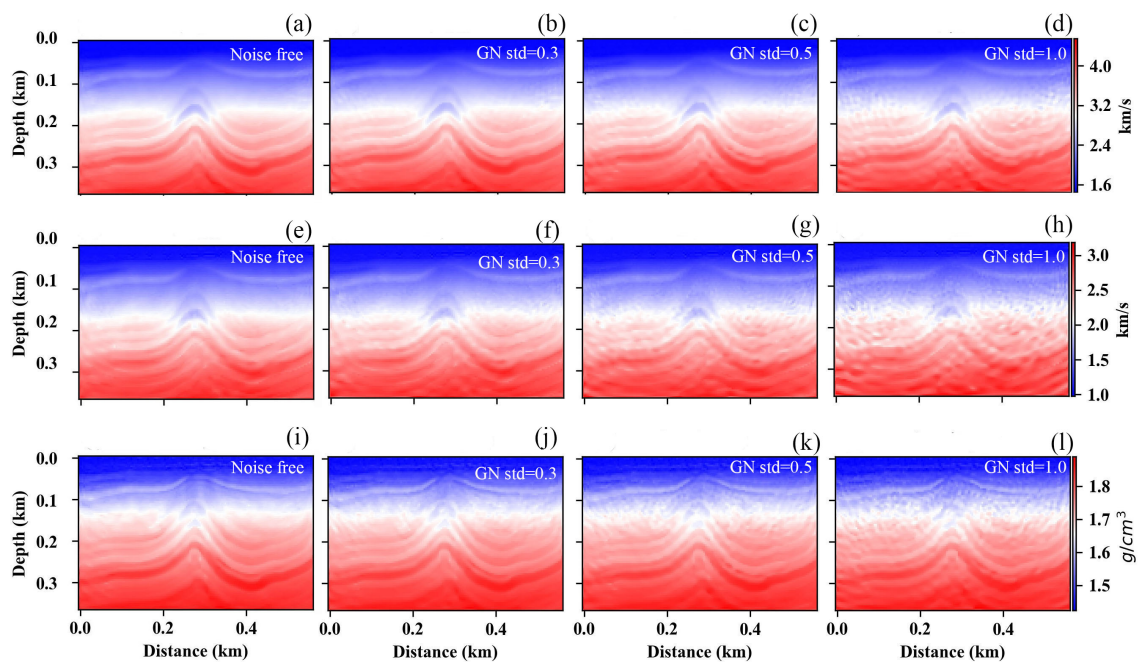


Figure 21: Random noise testing inversion results. (a),(e),(i), noise free inversion results for V_P , V_S , and density (b),(f),(j) Gaussian noise $std = 0.3$ inversion results for V_P , V_S , and density, (c),(g),(k) Gaussian noise $std = 0.5$ inversion results for V_P , V_S , and density, (d),(h),(l) Gaussian noise $std = 1.0$ inversion results for V_P , V_S , and density.